



**HAL**  
open science

# A comprehensive comparison of modeling strategies and simulation techniques applied in powder-based metallic additive manufacturing processes

Y. Jia, H. Naceur, Y. Saadlaoui, L. Dubar, Jean-Michel Bergheau

## ► To cite this version:

Y. Jia, H. Naceur, Y. Saadlaoui, L. Dubar, Jean-Michel Bergheau. A comprehensive comparison of modeling strategies and simulation techniques applied in powder-based metallic additive manufacturing processes. *Journal of Manufacturing Processes*, 2024, 110, pp.1-29. 10.1016/j.jmapro.2023.12.048 . hal-04800572

**HAL Id: hal-04800572**

**<https://hal.science/hal-04800572v1>**

Submitted on 24 Nov 2024

**HAL** is a multi-disciplinary open access archive for the deposit and dissemination of scientific research documents, whether they are published or not. The documents may come from teaching and research institutions in France or abroad, or from public or private research centers.

L'archive ouverte pluridisciplinaire **HAL**, est destinée au dépôt et à la diffusion de documents scientifiques de niveau recherche, publiés ou non, émanant des établissements d'enseignement et de recherche français ou étrangers, des laboratoires publics ou privés.

# A comprehensive comparison of modeling strategies and simulation techniques applied in powder-based metallic additive manufacturing processes

Y. Jia<sup>a,\*</sup>, H. Naceur<sup>a</sup>, Y. Saadlaoui<sup>c</sup>, L. Dubar<sup>b</sup>, J.M. Bergheau<sup>c</sup>

<sup>a</sup>INSA Hauts-de-France, CNRS, UMR 8201 - LAMIH, F-59313 Valenciennes, France

<sup>b</sup>Univ. Polytechnique Hauts-de-France, CNRS, UMR 8201 - LAMIH, F-59313 Valenciennes, France

<sup>c</sup>Univ. Lyon, ECL-ENISE – CNRS, UMR 5513 – LTDS, F-42023 Saint-Etienne, France

---

## Abstract

Additive manufacturing processes have been attracting extensive attention and developing greatly in recent years. These processes have been widely studied by industrial and academic. The manufactured parts are printed layer upon layer according to a computer-aided design model, hence very complex geometries can be created. Moreover, a wide range of materials (plastic, ceramic, metallic, etc.) can be used. Additive manufacturing processes require continuous analyses to investigate their performances and produce high-quality parts with minimal defects. The experimental approach is often used to assess these thermomechanical processes. However, it remains limited because of the exorbitant cost due to the numerous parameters. On the other side, numerical simulation can be an alternative solution to facilitate the optimization of the process parameters and predict the final characteristics of the manufactured parts with a reasonable cost. In the literature, numerous numerical methods and techniques have been developed and applied to simulate Additive manufacturing processes, such as Finite Element Method, Finite Volume Method, Lattice Boltzmann Method, Smooth Particle Hydrodynamics, Discrete Phase Method, etc. Depending on the objectives, different simulation scales have been developed (part scale, melt pool scale, powder scale, etc.). In this context, the proposed paper intends to present an overview of these numerical methods in order to provide a comprehensive comparison and a deep analysis of advantages and drawbacks among the available methods. Some promising techniques and future tendencies are also presented.

*Keywords* : Additive manufacturing; Numerical simulation; Heat transfer simulations; multiphysics; inverse identification

---

## 1. Introduction

Additive manufacturing (AM) attracts significant attention due to the possibility of using a large range of materials, such as aluminium [1], ceramics [2], and producing complex geometrical products [3; 4; 5]. Moreover, topology optimization can be conducted in part design to produce lightweight structure [6; 7; 8]. Additive manufacturing of metallic powder is the most widely reported and studied in the literature, such as directed energy deposition (DED) [9], directed metal deposition (DMD) [10; 11], selective laser melting (SLM) [12; 13], selective electron beam melting (SEBM) [14; 15], laser powder bed fusion (LPBF) [16], etc.

Despite the AM is considered as an industrial revolution in production method, the produced parts using this process are not free of defects, such as porosity [17; 18], brittle fracture [19], high residual stress [20; 21], undesired deflection [22], poor adhesion [23], etc. Therefore, optimization of the process parameters is often required to control the desired properties.

Improving the quality of manufactured parts using experimental approaches by trial and error are tedious and expensive, since there exist always several parameters involved in each AM process as shown in Figure 1. For example, in the SLM process, there are near twenty parameters which can be controlled. If each parameter requires a minimal of two tests, the total needed number of tests will be  $2^{20}$ . In addition, in-situ and ex-situ measurements are often tricky and

---

\*Corresponding author : [yabo.jia@uphf.fr](mailto:yabo.jia@uphf.fr)

cannot always provide the quantities of interest at all points of the part. Furthermore, opposed to the experimental results that designed for specific targets such as residual stress or microstructure, the numerical simulation provides a more flexible and cost-effective way to investigate the mechanism of defects in AM process. Thanks to the development of computing capabilities and numerical algorithms, numerical methods have nowadays become a key tool, which can provide an numerous and supplementary information to understand the physical problems regulating the AM processes.

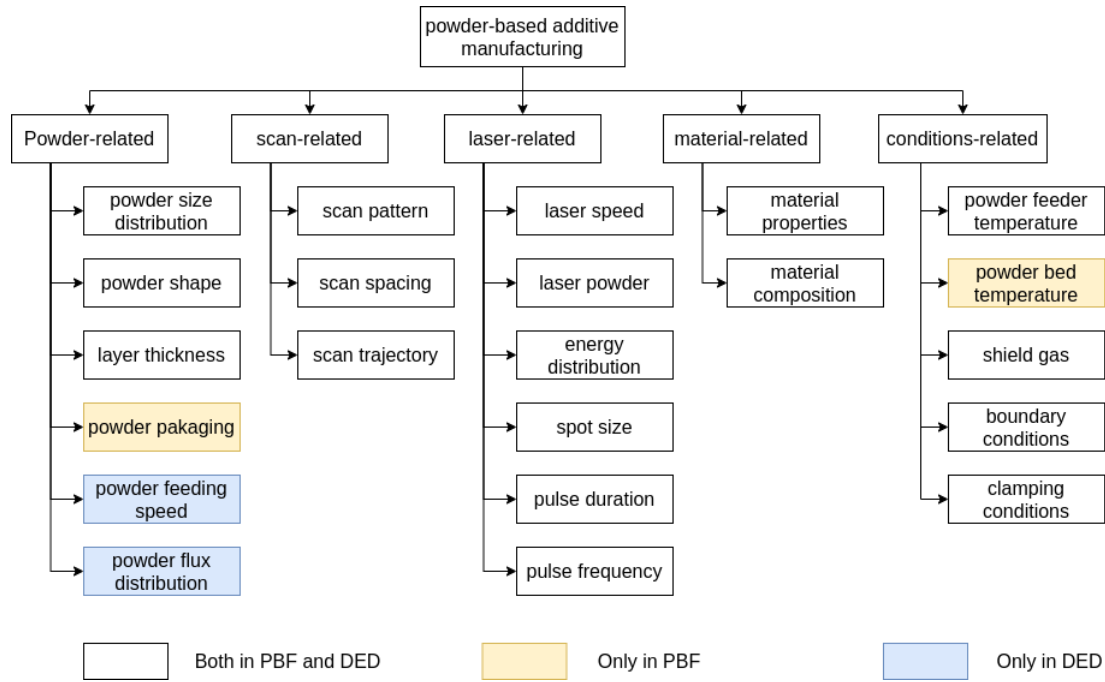


Figure 1: Process parameters in powder-based additive manufacturing.

In the last recent years, a large number of contributions have been emerging in the modeling of AM, spanning from microstructure models, dendrite and grain growth models, heat transfer models to multiphysics models and thermo-mechanical models. Numerous numerical methods such as analytical methods, Lattice Boltzmann methods (LBM), finite element method (FEM), finite volume element method (FVM) and others methods have been employed in AM simulations. As is known that numerical modeling of AM process has become a key tool, unfortunately, it is quiet difficult for engineers to select an adapted numerical methods and models, which allows providing the required numerical results with minimal computational cost. Therefore, understanding the physical phenomena behind the process and the capacity of different numerical methods is crucial for making decisions.

The review papers within some specific aspects of AM have also been presented in the literature. A review of part-scale finite element method in simulation of PBF has been presented by Luo and Zhao [24]. They summarized a full workflow from preprocessing to final post-processing, and different modeling techniques in FEM and their advantages and limitations are compared. Modeling techniques in meso/micro-scale model are illustrated by Körner and Markl [25]. Their discussions mainly focus on employing the numerical model to understand the mechanism of manufacturing issues. Similarly, Meier *et al.* [26] addressed some fundamental physical phenomena of SLM, and both experimental methods and numerical simulations are employed to establish the understandings of physical phenomena. King *et al.* [27] introduced their developments within Lawrence Livermore National Laboratory, and a multi-scale modeling strategy was described with LLNL developed codes (Diablo and ALE3D). Therefore, the review is mainly focus on explaining the capacities of their in-house codes and strategies to to optimize the additive manufacturing process. Bartlett *et al.* [28] provided an overview of residual stress in metal powder bed fusion, and they attended to assemble of knowledge existing in the literature regarding RS in PBF processes. Both numerical and experimental techniques for stress analysis are revised. Bertini *et al.* [29] conducted the similar analysis as Bartlett *et al.* [28] for stress formation. Cook *et al.* [30] reviewed the burgeoning literature concerning melt pool simulation, and the status of the

work published by leading research groups is also summarised. Relevant physics in BPF is described in great depth and detail. Wei *et al.* [31] presented the applications of transport phenomena models in the studies of heat and mass transfer models and the consequences laid on temperature field. The mathematical models related to physical phenomena are explained in detail and depth. Bayat *et al.* [32] summarised the pure conduction models, meso-scale models, powder-scale models, part-scale models and their applications, while allows grasping the current state-of-the-art and applications of these models.

Unlikely, the literature review of multi-scale and mutiphysics modeling work in DED is rarely reported, and one should note that modeling of DED is quiet complex due to the delivery system of powder and energy deposition. Pinkerton [33] provided a short review and advances in modeling of laser direct metal deposition in 2006. This review gives a clear illustration about the physical couplings that appear during DED operation. However, the modeling work presented is not up to date. Similarly, Guan and Zhao [34] presented the physical phenomena in DED and introduced some recent modeling work in DED. However, they barely touch upon residual stress modeling.

The primary objective of this article is to offer an extensive and up to date review of numerical models that have been developed to simulate powder-based additive manufacturing (AM) processes, including DED and powder bed fusion. The review spans a wide spectrum, ranging from micro-scale models to part-scale models, and covers diverse aspects including heat transfer models, multiphysics models as well as thermomechanical models. A comprehensive comparison of different modeling techniques at different scales is presented, which provides basic concepts of each technique and its objectives.

Figure 2 shows the two most widely-employed powder-based AM techniques. The main difference between two techniques is powder delivery system. Note that only DED and PBF will be used in the remaining sections for simplicity. PBF mainly employs the laser beam or electron-beam to melt the powder along the planned path, and the metal structure is built layer by layer [35; 36; 37]. The maximal dimensions of building part is limited by the building room. Compared to PBF process, the DED is more flexible since the powder metallic and energy will be projected directly to the desired positions. Therefore, DED allows to perform the repairing [38; 39; 40] and cladding operation [41].

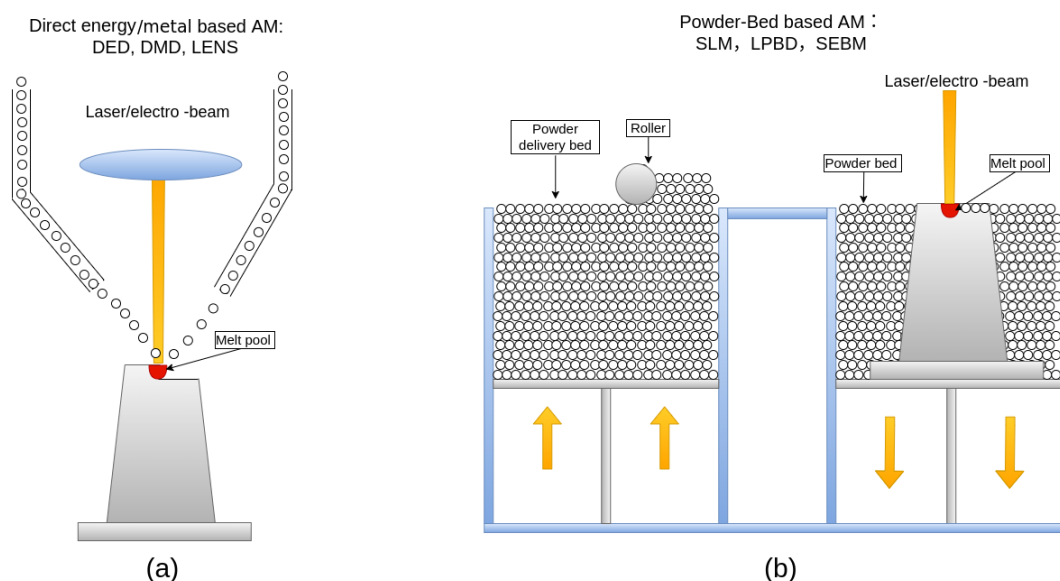


Figure 2: Two typical powder-based AM processes: directed energy/metal deposition (a); powder bed fusion (b).

The powder-based DED and PBF have numerous physical problems in common, which motivates us to review the modeling work. In this review, the first is to fill the gap of an overview of the state-of-the-art of relevant DED modeling work, and the different modeling technique is presented in detail. The second is to assess the different approaches to incorporate the physical effects that arise in DED and PBF modeling. The last is to compare the existing modelings approaches and their advantages and limitations.

The manuscript is organized as follows: In section 2, the physics and modeling scales involved in DED and PBF are

summarized. Both part-scale simulations and meso/powder-scale simulations are presented together, which allows understanding the fundamental difference in terms of involved physics. In section 3, the modeling techniques applied in part-scale simulations of DED and PBF are summarized together. Therefore, the simulations of DED and PBF are solved in the same ways, since the powder-related physics are disregarded. In section 4, a review of the meso/powder-scale models will be given, applied in DED and PBF simulations. The powder feeding systems of DED and PBF are different, thus their modeling are discussed separately. The conclusions and future work are in section 5.

## 2. The physics and modeling scales in DED and PBF

As it can be seen from figure 3, a summary of the multiphysics phenomena involved in PBF and DED processes are given. For simplicity, all the multiphysics phenomena involved in DED and PBF are listed together as follows :

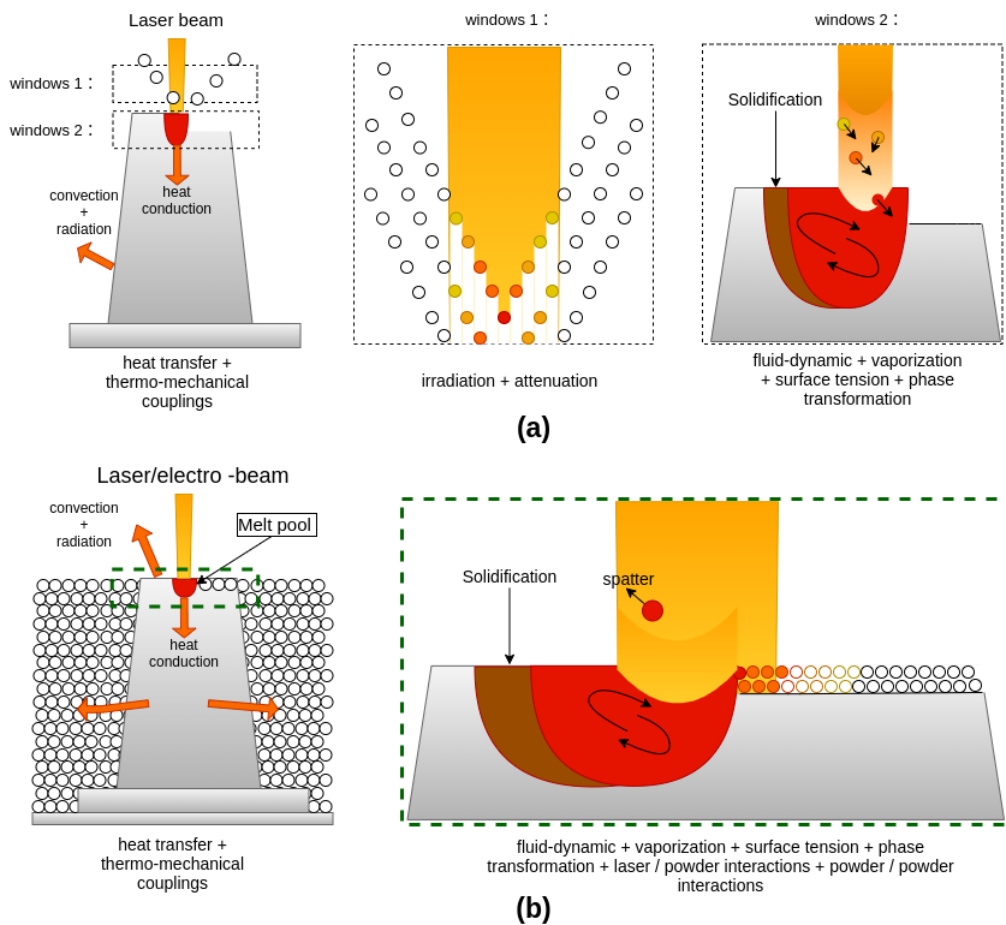


Figure 3: Schema illustration of multiphysics couplings in DED (a); PBF (b).

- (DED) interaction between carrier gas and powder.
- (DED) interaction between powder and laser, such as irradiation and attenuation.
- (PBF) multi-reflection of laser in powder bed.
- (PBF) powder packaging in powder bed.
- (DED/PBF) interaction between laser and substrate or existing layers.

- (DED/PBF) fluid-dynamic in melt pool include thermocapillary force, Marangoni force, Buoyancy force, Lorentz force and surface tension.
- (DED) effect of powder momentum when powder is injected to melt pool.
- (DED/PBF) heat transfer in building part and heat losses due to convection and radiation.
- (PBF) heat transfer in powder bed.
- (DED/PBF) possible recoil pressure effect due to vaporization.
- (DED/PBF) microstructure : grain growth, metallurgical transformation during manufacturing.
- (DED/PBF) distortion and residual stress in building parts.

According to requirements, not all the physical problems presented above should be taken into account, and some assumptions can be made for simplifying numerical models. Part-scale and meso/powder-scale multiphysics modeling are different ways to simulate AM processes. Part-scale models are designated to investigate the macro-scale consequences induced by the process, such as the fusion profile of multi-pass and multi-layer, residual strain/stress, and phase transformation in solid. While Meso/Powder-scale models investigate the multiphysics couplings due to the interactions concerned in the process, such as fluid-dynamic, heat and mass transfer. Figure 4 shows a comparison of multi-scale and multiphysics simulations, and these models can be classified according to the governing equations and discretization scale.

- Part-scale models consist in solving heat transfer equations, possibly coupled with metallurgy transformation equations. The modeling techniques are quite similar to those developed in the context of welding simulations, especially, the part-scale modelings in FEM are widely used since these models have been implemented in commercial software, such as Abaqus<sup>®</sup>, Ansys<sup>®</sup>, Sysweld<sup>®</sup>, Marc-Mentat<sup>®</sup>, etc. Therefore, part-scale models are equally capable to investigate the heat transfer and residual strain/stress [42]. However, over-simplified assumptions related to powder/energy feeding and fluid-dynamic in melt pool lead to low precision of numerical predictions, and the track shape are generally predefined in preprocessing stage. Thus, the part-scale models are generally carried out after the experiments, and the experimental results (melt pool shape, thermal-cycles) are fed to calibrate the thermal models. Once the thermal models give satisfactory precision, the results are used as the input of mechanical simulations.
- Meso-scale modeling mainly focuses on the melt pool simulation, and the powder particles are simplified by continuum layer (in PBF) or mass flux distribution (in DED). The meso-scale models allow considering the effects of fluid dynamic and surface tension, which can make a relative high-fidelity prediction of track shape and temperature fields. The simplifications made for powder particles can greatly reduce the computation cost, as it can use a relatively coarse mesh/grid for discretization. However, the defects related to powder-related parameters cannot be investigated by meso-scale models.
- Powder-scale modeling focus not only on melt pool but also on the interaction between powder and laser, which allows understanding the effect of process parameters on stability of melt pool [43], heat and mass transfer in melt pool [44], free surface evolution and defects formation [45]. However, these type of simulations are extremely computational expensive.

### 3. Part-scale thermal-mechanical modeling

The numerical methods of part-scale modeling in FEM are mainly adopted from the techniques developed for multi-pass welding simulations [46; 47; 48; 49], and figure 5 shows a schema of modeling flow in part-scale simulations. The simulation are carried out in two steps: (i) a heat transfer simulation is first carried out to determine the temperature distributions during the process, and a strong coupling between temperature and phase transformation. The simulation of metallurgy transformation in solid is not always mandatory. (ii) the temperature evolution and phase proportions

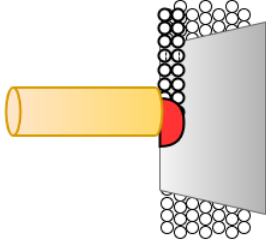
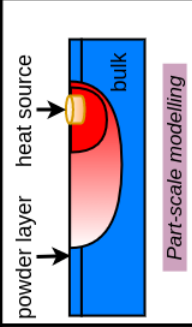
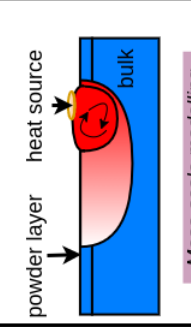
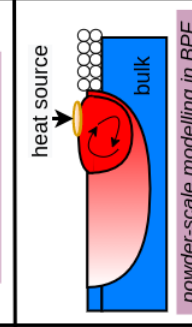
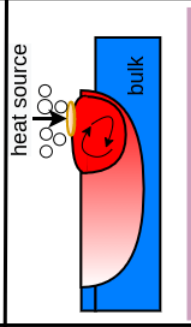
Processes	Inputs:	Models:	Governing equations	Intermediate outputs:	Capacities
	<b>powder feeding:</b> pre-defined thickness continuum medium <b>energy feeding:</b> calibrated 2D or 3D heat source		heat conduction equation	temperature results + metallurgy transformation in solid	1. melt pool size 2. metallurgy phase transformation 3. grain shape/size
	<b>powder feeding:</b> continuum medium + mass flux distribution (DED) <b>energy feeding:</b> 2D heat source + ray tracking in case of keyhole		mass conservation equation + energy conservation equation	temperature results	1. melt pool size 2. metallurgy phase transformation 3. grain shape/size 4. free surface 5. keyhole 6. vaporization
	<b>powder feeding:</b> discretization of powder bed <b>energy feeding:</b> 2D heat source or ray tracking in powder bed or keyhole		energy conservation equation + navier-stocks equation	<i>fluide dynamic</i> 1. mass conservation 2. energy conservation 3. bouyancy 4. marangoni effect 5. surface tension 6. solidification 7. recoil pressure 8. free surface tracking	1. melt pool size 2. metallurgy phase transformation 3. grain shape/size 4. free surface 5. keyhole 6. vaporization
	<b>powder feeding:</b> mass flux distribution or powder particle + particle temperature <b>energy feeding:</b> laser attenuation		free surface tracking in volume of fluide method	7. pores formation 8. rough surface 9. spatter	high-fidelity models

Figure 4: Resume of multi-scale and multiphysics simulations.

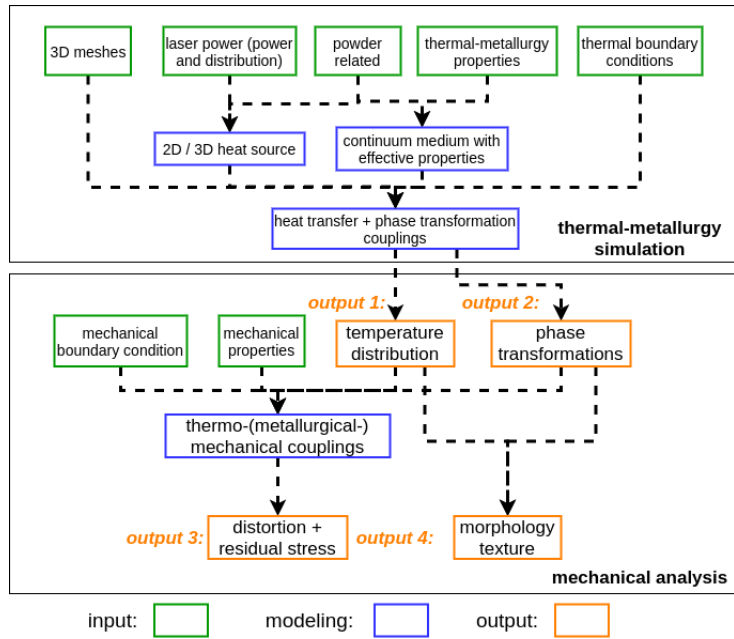


Figure 5: An example of part-scale modeling flow in FEM.

calculated are imposed as loading conditions in a mechanical simulation; and complex thermo-elastoplastic or thermo-elasto-viscoplastic constitutive laws are generally used to predict residual stresses and distortions. Figure 6 resumes the couplings of several physical phenomena and features that appeared in figure 5 : heat transfer, metallurgical transformations, and mechanical stresses and strains. The feed-backs of mechanical results upon heat transfer and metallurgy transformation are generally neglected, since the energy dissipation due to plastic deformation is negligible to energy input induced by the processes.

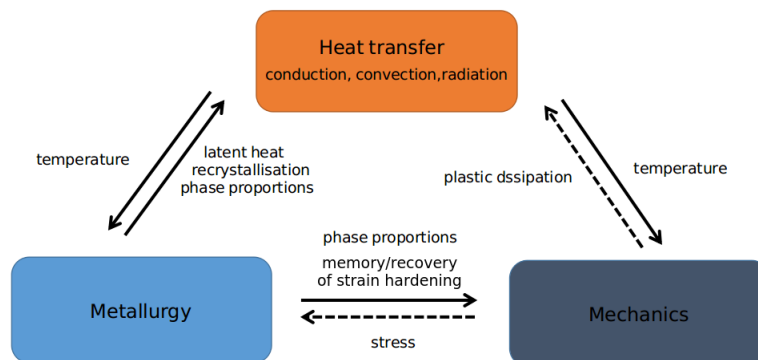


Figure 6: multiphysics couplings during welding processes. Dotted arrows denote effects disregarded most of the time [50].

Part-scale modeling in FEM mainly consists in simulating : mass addition (Section 3.1), thermal analysis (Section 3.2), and thermo-mechanical analysis (Section 3.3).



### 3.1. Mass addition simulation

In FEM, since the element volume stands for the material volume, hence metal deposition is simulated by activating the death/quiet element, adding new element or increasing the volume of existing element.

#### 3.1.1. Quiet and inactive element method in PBF and DED

Modeling the metal addition in AM process is quite similar to modeling multi-pass welding [51; 52; 53; 54]. The metal deposition in AM can be achieved by using quiet elements [55; 56; 57; 58] or inactive elements [59; 60; 61; 62]. These two approaches require a predefined deposit mesh, and the powder or metal deposited are considered as continuum media.

The quiet element method assign artificial properties that do not affect the analysis results, and quiet element will transfer to active element once the temperature of quiet element is over temperature fusion. For heat transfer analyses, a scaling factors will be used to adjust the thermal properties of quiet element so that the influence of exiting quiet element can be minimized :

$$\begin{aligned} k_{quiet} &= s * k_{active} \\ C_{p_{quiet}} &= s * C_{p_{active}} \end{aligned} \quad (1)$$

where  $k_{quiet}$ ,  $C_{p_{quiet}}$ ,  $k_{active}$ ,  $C_{p_{active}}$  are the thermal conductivity and specific heat for quiet element and active element respectively.  $s$  is the scaling factor.

Similarly, for mechanical analysis, Young's modulus of quiet element is defined as :

$$E_{quiet} = E_{tf} \quad (2)$$

where  $E_{tf}$  is Young's modulus similar to the hot material of active element, so that the quiet element does not disturb the overall response of the structure.

The quiet element method presents advantages, such as easy-implementation in commercial FE codes via user subroutines and without requiring equation renumbering and solver initialization during the simulation, since the number of degrees of freedom (DOF) is the same. However, the scaling factor  $s$  in equation 1 should be small enough but cannot be too small to result in ill-condition of Jacobian. Furthermore, modeling AM with quiet element method could be time-consuming, because most of the analysis domain is composed of quiet elements, which may lead to high computation time.

In inactive element method, inactive elements are not included in the simulation until the corresponding metal has been added. Activation of elements is generally controlled by a time-space function. For example, Fanicchia *et al.* [63] have applied inactive element method for deposit shape prediction (see from figure 7). Compared to quiet element method, inactive element method do not suffer errors or ill-conditioning introduced by scaling factors, and only nodal DOFs of active element are considered. Therefore, a smaller algebraic system by the Newton-Raphson linearization is expected. However, the frequent equation numbering and solver initialization, due to the new active element at each time step, would hide the computational advantage of solving for a reduced active number of DOFs.

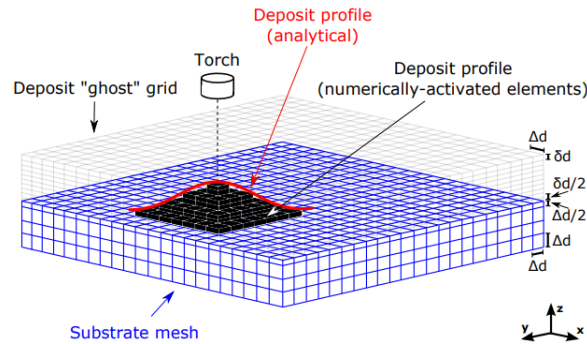


Figure 7: Application of inactive element method for metal deposition simulation [63].

Michaleris [57] has provided a full investigation of two techniques, he demonstrated that both methods can give equivalent results if they are implemented properly. A hybrid quiet inactive metal deposition method has also been proposed by Michaleris. Inactive element layers could largely reduce active number of DOFs and quiet element within layer require equation numbering and solver initialization only one time per layer. Thus, the hybrid quiet inactive method could accelerate computation time. This hybrid method has been applied for wall build and LENS simulations (see from figure 8).

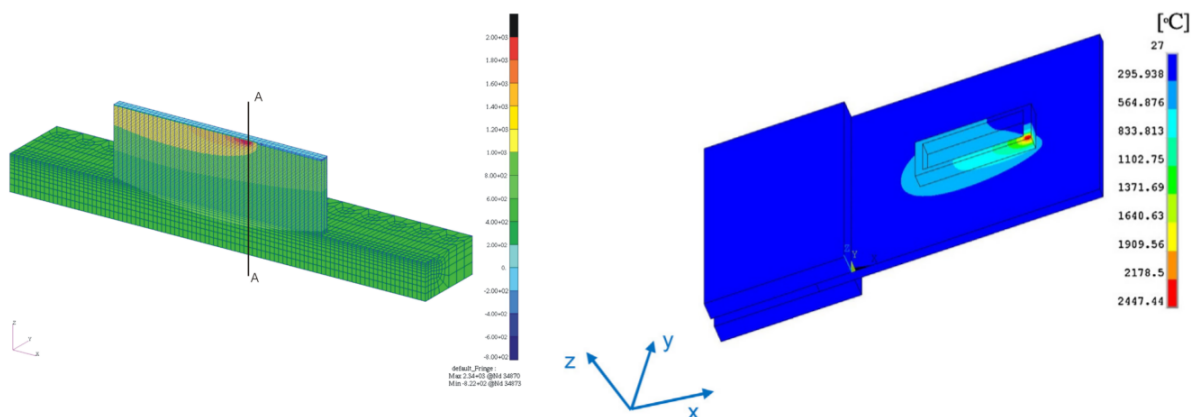


Figure 8: Application of hybrid method for simulating wall build [57] and LENS [64].

### 3.1.2. Other metal deposition methods in DED

In quiet or inactive element method, the mesh has been defined in preprocessing and the element is switched to be active once the metal is deposited. Other metal deposition methods model the geometry built-up by adding new elements to substrate or increasing volume gain of existing element.

Taberero *et al.* [65] has proposed a geometrical model to simulate laser cladding process, and modeling of cladding process is quit similar to that of DED. Therefore, the laser cladding will be considered as an example. As it can be seen from figure 9, the input data of geometric model are the results given by powder concentration model [66] and thermal model [67]. The thermal model will first predict the melting pool geometry, and powder mass distribution at the surface of substrate is simulated by concentration model. Prediction of metal deposition is achieved by calculating a mass balance that captured by the melt pool.

The mass of the resulting clad is equal to the mass of the injected powder at each point of the melting pool and the height of new added element is calculated from :

$$m_{\text{clad}} = \eta_p * m_{\text{injected}} \quad (3)$$

$$60,000 \cdot \Phi_i \cdot \Delta s^2 \frac{\Delta s}{V_f} = \rho \cdot \Delta s^2 \cdot h_i$$

where  $\Phi_i$ ,  $\Delta s$ ,  $V_f$ ,  $\rho$ ,  $\eta_p$  are powder concentration, node length, cladding nozzle feed rate (in millimeters per minute), powder material density and powder catchment efficiency. Here,  $\Delta s^2$  is the area of each discrete element.

Feulvarch *et al.* [68] proposed an original formulation to simulate molten metal deposition geometry with a very low CPU time. This new approach is based on the original technique proposed by Leblond *et al.* [69] for the incorporation of surface tension in finite element calculations. At each time step, the metal deposition is simulated by inflating of 2D mesh, and volume gain is controlled by the volume flux of material added. Then, a computation of balance of stress on the same 2D mesh is carried out by considering the interaction between the curvature effect of the surface tension and the pressure difference between the molten zone and the atmosphere. Figure 11 shows some applications to simulate shape of metal deposition.

Compared to changing volume gain of existing element, the technique based on adding new elements do not suffer from the problem of divergence related to mesh distortion. However, the new added elements conduct frequent

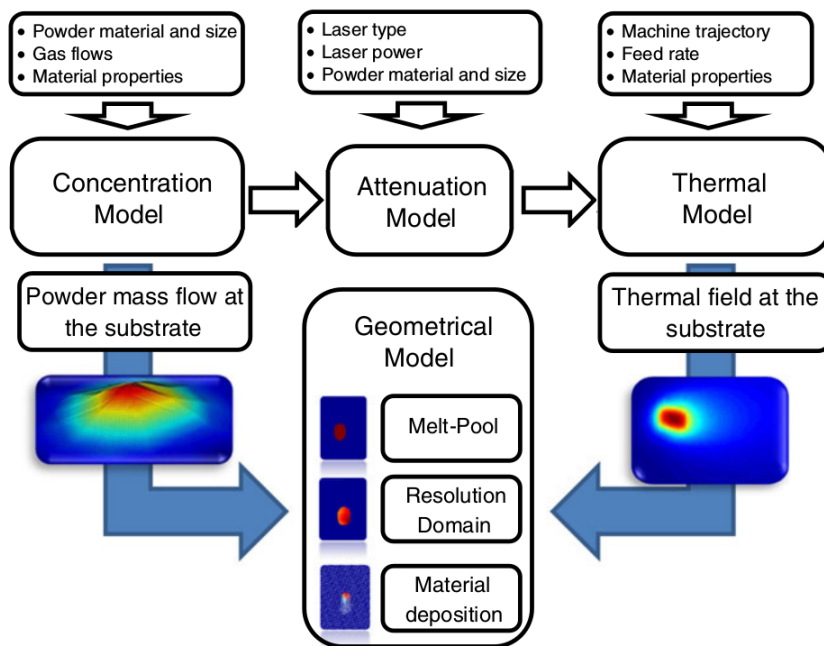


Figure 9: Resolution algorithm scheme of the complete model for laser material deposition process [65].

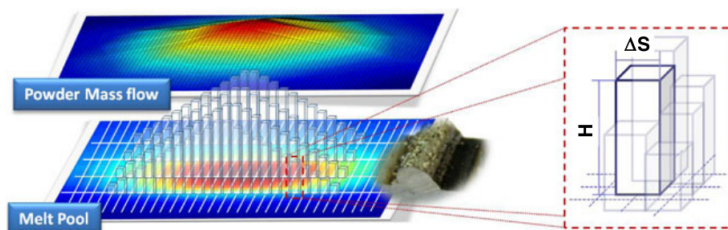


Figure 10: Model approach and clad discretization starting from powder concentration and melt pool shape [65].

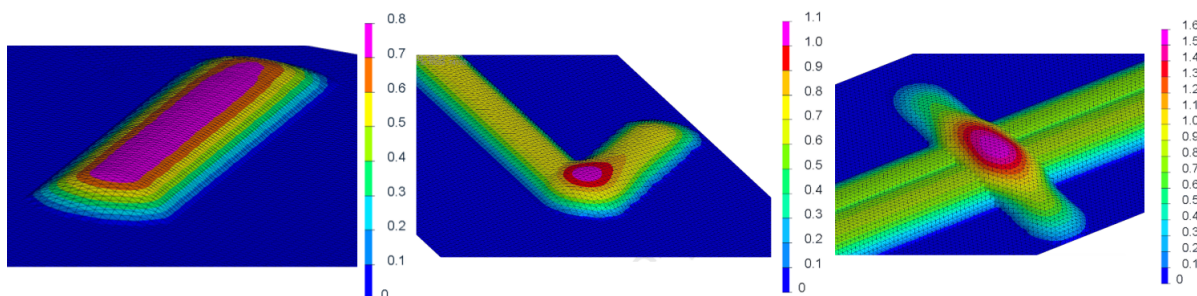


Figure 11: Shape of metal deposition: single track (left); clad corner (center); clad overlapping (right). [68].

equation numbering and solver initialization for each time step, which will slow down the simulation. Furthermore, the non-conform mesh due to new added elements generally leads to difficulties in the thermal and mechanical analyses.

### 3.2. Thermal analysis

In heat conduction simulation, only conservation of energy should be solved. The governing equation of heat transfer, coupled with metallurgical transformation, can be expressed:

$$\rho C \frac{\partial T}{\partial t} = \frac{\partial}{\partial x} \left( K_{xx} \frac{\partial T}{\partial x} \right) + \frac{\partial}{\partial y} \left( K_{yy} \frac{\partial T}{\partial y} \right) + \frac{\partial}{\partial z} \left( K_{zz} \frac{\partial T}{\partial z} \right) + q$$

with:  $\lambda \nabla T \mathbf{n} = q(T, t)$  on  $\partial\Omega_q$

$$T = T_p(t) \quad \text{on } \partial\Omega_T^q$$

and  $\partial\Omega = \partial\Omega_q \cup \partial\Omega_T$

(4)

where  $\rho = \sum_{phases} p_i \rho_i$ ,  $K = \sum_{phases} p_i K_i$  and  $C = \sum_{phases} p_i C_i$ .  $p_i$ ,  $\rho_i$ ,  $K_i$ ,  $C_i$  are, respectively, the proportion of phase, the density, conductivity and specific heat.  $K_{xx}$ ,  $K_{yy}$ ,  $K_{zz}$  represent the thermal conductivity of X, Y, and Z directions respectively.  $T$  is the temperature at nodes, and  $q$  is a function presented in section 3.2.1 to describe heat flux. The enthalpy related to phase transformation (solid/liquid) can be considered by applying the apparent heat capacity method [70].

$$C_{modified} = \begin{cases} C & \text{if } T < T_m - 0.5\Delta T \\ C + 2L/\Delta T & \text{if } T_m - 0.5\Delta T < T < T_m + 0.5\Delta T \\ C & \text{if } T > T_m + 0.5\Delta T \end{cases}$$
(5)

where  $C$  and  $L$  represent specific heat and latent heat, and  $\Delta T$  is the difference absolute between solid and liquid temperatures.

The initial conditions can be expressed as:

$$T(x, y, z)|_{t=0} = T_0$$
(6)

The convective and radiative losses on free surface are calculated by following:

$$\begin{aligned} q_{conv} &= h_{conv} (T - T_{air}) \\ q_{rad} &= \sigma \epsilon (T^4 - T_{air}^4) \end{aligned}$$
(7)

where  $h_{conv}$ ,  $\sigma$ ,  $\epsilon$  are respectively coefficient exchange with air, Stefan-Boltzmann constant and the surface emissivity.

#### 3.2.1. Heat source modeling in DED and PBF

As it can be noticed from figure 5, the heat transfer simulations neglect fluid-dynamic in melt pool for reducing computational cost in part-scale modeling, the interaction between powder and laser is general simplified by a Gaussian 2D/3D heat source. Therefore, the selected heat source model should be able to produce a correct melt pool and thermal cycles that are observed in the experiments. Some representative heat flux models applied in AM simulations with different features are summarized in Table 1.

Figure 12 presents the energy distribution of the representative heat source. The surface heat flux (Figure 12-(a)) is the most simple but widely used in SLM simulation [77; 78; 79] or laser welding simulation, since the laser energy distribution can be measured directly by wattmeter [86]. Surface heat flux is suitable to simulate conduction mode with a low depth to width ratio (little than 0.5) of the molten pool or low energy input that is calculated from  $\frac{P}{V}$ , where the heat transfer effect related to fluid-flow in melt pool can be ignored.

Some research has been carried out to investigate the relative importance of convective heat transfer over conductive heat transfer [87; 88; 89; 90]. Peclet number or empirical quantity (MP) proposed by Arrizubieta [90] have been used to quickly evaluate the significance of molten metal convection, however, these methods are useful only for a certain set of process conditions or specific materials and need further research.

Table 1: Some basic heat source models

Heat source	Heat flux equations	Reference
Surface heat flux	$q(x, y) = \frac{A \times P}{\pi r_0^2} \exp\left[-B \left(\frac{x^2 + y^2}{r_0^2}\right)\right]$ <sup>(1)</sup>	[71; 72; 73; 74; 75]
3D conical heat flux	$q(x, y, z) = A \times Q_0 \exp\left[-\frac{x^2 + y^2}{(R_t - (R_t - R_b)(z_t - z)/(z_{tdouble} - z_b))}\right]$ <sup>(2)</sup>	[76; 77; 78; 79]
3D cylindrical heat flux	$q(x, y, z) = A \times Q_0 \exp\left[-\frac{x^2 + y^2}{r_0^2}\right]$ for $z \in [z_b, z_t]$	[78; 79; 80]
Double ellipsoidal heat flux	$q_{f,r}(x, y, z) = \frac{6\sqrt{3fQ_{f,r}}}{abc_{f,r}\pi\sqrt{\pi}} \exp\left(-\frac{3z^2}{c_{f,r}^2} - \frac{3x^2}{a^2} - \frac{3y^2}{b^2}\right)$ <sup>(3)</sup>	[78; 79; 81; 82]
Optical penetration depth based heat flux	$q(x, y, z) = \frac{A \times q(x, y)}{\delta} \times \exp\left(-\frac{ z - z_{surface} }{\delta}\right)$ <sup>(4)</sup>	[73; 83]
Monte Carlo based heat flux (electron beam)	$q(x, y, z) = Q \times \left[ \frac{1}{\delta \cdot \int_{-\frac{z_0}{\delta}}^{+\infty} \exp(-t^2) dt} \exp\left(\frac{(z - z_0)^2}{\delta^2}\right) \right]$ <sup>(5)</sup> $\times \left[ \frac{N}{\pi r_0^2} \exp\left(-N \cdot \frac{(x - x_s)^2 + (y - y_s)^2}{r_0^2}\right) \right]$	[84]
Rotatory Gaussian body heat flux	$q(x, y, z) = \frac{9Q}{\pi h r_0^2} \cdot \exp(\beta I_f z) \cdot \exp\left(\frac{9r^2}{r_0^2 \cdot \log(z/h)}\right)$ <sup>(6)</sup>	[85]

<sup>(1)</sup>  $A$  laser absorption coefficient,  $P$  the laser power,  $r_0$  the laser spot radius,  $B$  shape factor of the Gaussian distributed heat flux (typical value is 2).

<sup>(2)</sup>  $q_0$  the maximum intensity,  $R_t$  and  $R_b$  are spot radius at upper and lower planes,  $z_t$  and  $z_b$  are z-coordinate of upper and lower planes.

<sup>(3)</sup> the front and rear part denoted by subscripts  $f$  and  $r$  respectively.

<sup>(4)</sup>  $\delta$  is penetration depth.

<sup>(5)</sup>  $Q$  the beam power,  $z_0$  the location with the highest energy density,  $N$  the concentration coefficient of the electron beam,  $x_s$  and  $y_s$  the coordinates of the center of the beam.

<sup>(6)</sup>  $U$  the accelerate voltage,  $I$  the beam current,  $N_0$  effective power coefficient,  $h$  the effective affecting depth of electron beam,  $\beta$  ranges from negative values to positive values as focused conditions varies,

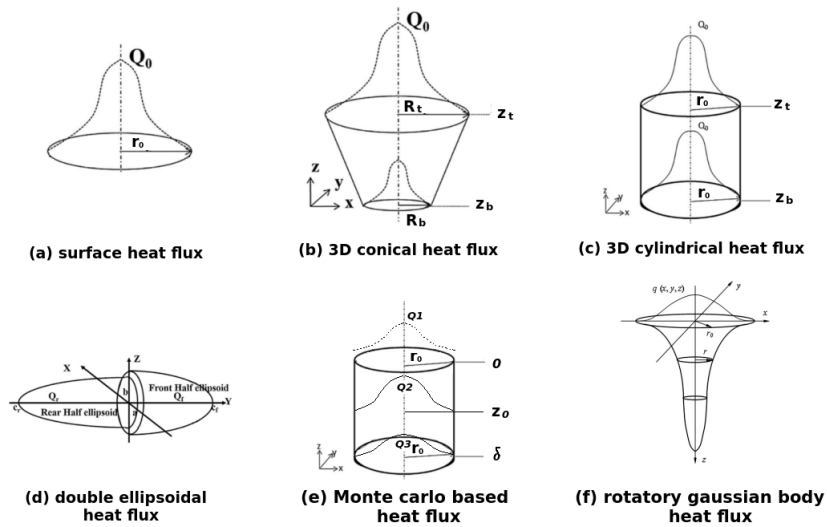


Figure 12: Representative heat flux models, adapted from [78; 81; 84; 85].

As the fluid-dynamic in melt pool is neglected in heat conduction simulation, two techniques are available to consider that effect:

1. The 3D heat flux: the volume of heat source can simulate the effect of fluid dynamic in melting pool.
2. The equivalent thermal conductivity technique [91; 92]: enhanced heat conduction in melt pool by arbitrary increasing the values of thermal conductivity over temperature fusion.

Defining a satisfactory 3D heat flux to perfectly compensate the neglected heat convection is not easy. One way is to following the modelisation experience [78; 81; 84; 85] reported in the literature. Another simple way is to identify the source distribution from the melt pool shape, and this method has been widely used in laser welding simulation. Figure 13 shows two examples of macrographs of laser welding, and the heat source should be able to reproduce the shape of fusion zone (FZ) and the heat affected zone (HAZ). In the first figure, a 3D conical heat flux is enough to obtain a good melt pool shape. In the second figure, a 3D conical heat flux allows producing the good shape of HAZ, while the combination of 3D conical and 3D cylindrical heat flux can simulate the particular nail-head shape of the melt pool. One should note that if the aim is to obtain a satisfactory temperature field in the solid phase, the 3D conical heat source is sufficient. Otherwise, the combination heat source should be used and gives better precision in predicting melt pool shape [78], however, two times more parameters need to be calibrated.

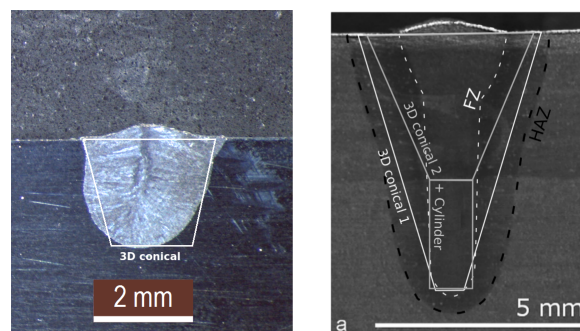


Figure 13: Schema of heat source definition, adapted from [86; 93].

A combination of both techniques has also been reported in the literature [94], while applying both of them results in more parameters (parameters of heat source and parameters of enhanced factors).

In FEM simulation, fitting the heat source parameters is the most important and time consuming step, since the temperature field simulated is responsible for the microstructure, phase transformation, and mechanical consequence. Automatic parameter calibration procedure (inverse method) has been developed for double ellipsoidal [95; 96] and combination of surface and 3D cylindrical [97] for welding simulation, which can also be used for modeling DED and PBF. However, these procedures are generally applicable for single source or combined heat source less than 5 parameters.

### 3.2.2. Continuum medium with effective properties in PBF

The powder bed in PBF is treated by continuum medium [98; 99; 100]. Therefore, effective density and thermal conductivity of powder layer are calculated from porosity of powder bed and properties of bulk [101; 102; 103; 104]. The effective properties of powder bed are the most important ones since they play an important role in predicting temperature distribution. Thermal conductivity for solid substrate and powder bed are significantly different, as gas in the pores can strongly reduce the thermal conductivity in metallic powder bed. To model this effective thermal conductivity, several techniques have been proposed [105; 106; 107] and two mostly used techniques are detailed. In simulation of SLM 316L, Antony *et al.* [108] adopted the equations 8 to calculate effective density and effective thermal conductivity. The effective density is estimated based on the assumption that all the solid particles in the powder layer are spherical in shape and equal in size and densely arranged in a cubic array [109]. The effective thermal conductivity is deduced considering the gas embedded within the voids of the powder bed given by Bugada *et al.* [110].

$$\begin{aligned}\rho_{powder} &= \frac{\pi\rho_{bulk}}{6} \\ k_{powder} &= \frac{\rho_R k_{bulk}}{(1 + \Phi(k_{bulk}/k_g))} \\ \text{with } \Phi &= 0.02 * 10^{2(0.7-\rho_R)}\end{aligned}\quad (8)$$

where  $\rho_R$ ,  $k_{bulk}$ ,  $k_g$  are the initial relative density of the powder layer, temperature dependent thermal conductivity of bulk, thermal conductivity of the surrounding gaseous environment (0.0260 W/MK).

Equation 9 has been applied to describe properties of powder bed [103; 111], which only depends on local density of the powder bed. The powder density, thermal conductivity and specific heat can be calculated from

$$\begin{aligned}\rho_{powder} &= (1 - \tau) * \rho_{bulk} \\ k_{powder} &= (1 - \tau)^n * k_{bulk} \\ C_{powder} &= C_{bulk}\end{aligned}\quad (9)$$

where the  $\tau$  is the porosity of powder and  $n$  is the empirical parameter, which is taken as 4 in general.

During the simulation, the effective properties of powder bed can depend on the temperature, and a piece-wise model for thermal conductivity was modeled as [103; 111]

$$P_{eff} = \begin{cases} P_{powder}(T), T_0 \leq T \leq T_s \\ \frac{P_{bulk}(T_m) - P_{powder}(T_s)}{T_m - T_s} (T - T_s) + P_{powder}(T_s), T_s < T < T_m \\ P_{bulk}(T), T \geq T_m \end{cases}\quad (10)$$

with sintering temperature  $T_s$ , melting temperature  $T_m$ .  $P$  represents  $k$  and  $\rho$ . Furthermore, during the cooling stage, the powder state elements heated over melting temperature, thus the initial powder state elements should be irreversibly changed to the solid state elements with the properties of bulk.

An example of SLM Inconel 718 with laser power of 100 Watt and speed of 200 mm/s is carried out. The thickness of powder layer is 40 micro, and different effective thermal conductivity values have been tested. Temperature-dependent  $k_{bulk}$  and laser absorptivity taken from [112]. A steady-state simulation is conducted by *SYSWELD* [113; 114], and powder to solid transformation is handled by metallurgy module. Figure 14 shows the properties of powder bed calculated from aforementioned methods. The density of powder bed given by Eq. 8 and Eq. 9 is almost the same, while the conductivity of powder predicted by Eq. 9 is about three times larger than that predicted by Eq. 8.

Figure 15 gives the contours of steady temperature. First, the isotherms in Figure 15-(b) and Figure 15-(c) are quiet similar, which means that the properties estimated by Eq. 8 and Eq. 9 have the comparable impact. Second, compared to

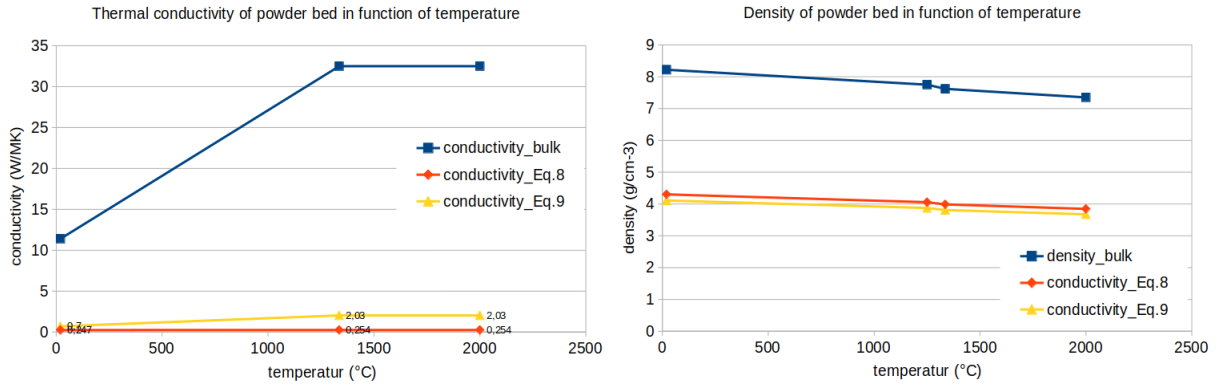


Figure 14: The thermal conductivity and density of powder bed calculated from different methods.

Figure 15-(a), one can conclude that application of effective properties plays an important role in predicting steady-state temperature. Table 2 shows the comparison of melt pool size, and we can conclude that the melt pool is significantly underestimated without using effective properties, since the energy can diffuse easily in the powder bed.

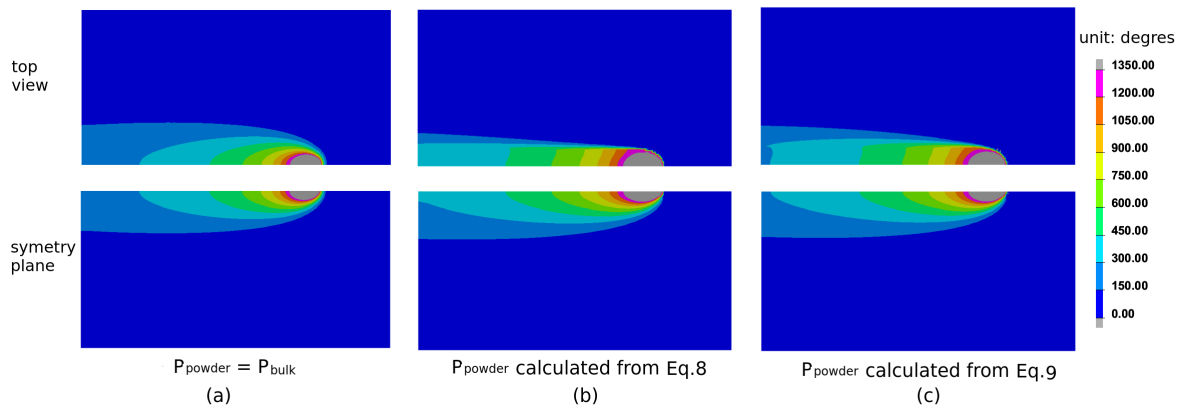


Figure 15: Effect of effective properties of powder layer on steady temperature distribution:  $P_{powder} = P_{bulk}$  (a);  $P_{powder}$  calculated from Eq. 8 (b);  $P_{powder}$  calculated from Eq. 9(c).

Table 2: Melt pool size simulated by different models (unit: [mm]).

	figure 15-(a)	figure 15-(b)	figure 15-(2)
length	0.199	0.250	0.244
width	0.133	0.185	0.168
depth	0.059	0.066	0.064

Ahsan *et al.* [115] has conducted the experiments to measure the effective thermal conductivity of powder bed of different materials, such as Inconel 718, Ti6Al4V, SS 316L, SS 304L and CoCrMo. Experimental results show that the thermal conductivity varies from 0.35 W/m.k (400 degree) to 0.51 W/m.k (1100 degrees) for all the materials. The thermal conductivity of powder bed increases slightly with increasing temperature, while this augmentation of thermal conductivity is negligible compared to the thermal conductivity of bulk.

To conclude, the properties of powder bed measured by experiments are complex, and measurement shows the conductivity is significantly lower than that of bulk material. The numerical results shows the powder bed properties play an important role in predicting melt pool and steady temperature. Therefore, both Eq. 8 and Eq. 9 can be used to



rapid estimation of powder bed properties.

### 3.2.3. Phase transformation modeling in DED and PBF

Various models have been developed for phase transformation in welding processes, and these models can be directly applied in AM simulations. Several classical and mostly used phase transformation equations of steel are introduced here:

1. The Leblond equation [116] is usually used for modeling the ferrite to austenite transformation (during the heating):

$$\dot{p}(T) = \frac{dp(T)}{dt} = f(\dot{T}) \frac{p_{eq}(T) - p(T)}{\tau(T)} \quad (11)$$

where  $p_{eq}$  is the equilibrium phase fraction.  $\tau$  is the delay time as a function of the temperature.  $\dot{T}$  is heating or cooling rate.  $p$  is the proportion of phase and  $t$  is time.

2. Koistinen-Marburger equation [117] is mainly used to describe the austenite to martensite transformation:

$$p_m(T) = p_m (1 - \exp(-b(M_s - T))) \quad (12)$$

with  $p_m$  is the phase fraction at ambient temperature, and  $b$  is a coefficient value that depends on the carbon steel.  $M_s$  is the temperature that martensite starts forming.

For other materials, such as Titanium alloy and Aluminium alloy, still need more research in modeling phase transformation, as these materials are widely used in AM.

### 3.3. thermo-mechanical analysis

The thermo-mechanical analysis of AM is quite similar to multi-pass welding simulations. The metal deposition technique has been presented in Section 3.1, generally, and the mesh in thermal analysis will be used directly in mechanical simulation.

The non-linear mechanical analysis in AM is solved in static, and the equilibrium equation is expressed as:

$$\nabla \cdot \sigma + \mathbf{f} = 0 \quad (13)$$

where  $\sigma$  is Cauchy stress tensor and  $\mathbf{f}$  is the body and surface forces.

The total strain  $\varepsilon_{total} = \frac{1}{2} (\text{grad } \mathbf{u}^* + \text{grad}^T \mathbf{u}^*)$  induced by the process can be described as the sum of elastic strain  $\varepsilon_{elastic}$ , (visco)plastic strain  $\varepsilon_{plastic}$ , and thermal strain  $\varepsilon_{thermal}$ , and the plastic behavior of metallic general follows  $J_2$  plasticity.

The thermo-mechanical responses in AM are also widely studied, and the studies mostly performed with the time-independent behavior [42; 118; 119]. Chen *et al.* [120] has applied thermo-mechanical-metallurgical model to simulate the formation of microstructure and residual stress in DED. Strain rate independent model is presumably for ease of implementation and to reduce computation time, but such models disregard annealing behavior, or stress and plastic strain relaxation at elevated temperatures [121]. In fact, few studies have assumed the elastic-perfectly plastic condition in AM simulations.

Kotkunde *et al.* reported that an important strain rates between  $10^1$  and  $10^{-2} \text{ s}^{-1}$  have been measured experimentally [123]. Similarly, experimental results of Ganeriwala [121] *et al.* also shows an important strain-rate dependence and annealing behavior of Ti-6Al-4V at elevated temperature (see figure 16). Since AM process associates with rapid cooling and heating sequences as well as high temperature, thus, some authors [121; 124; 125] think that it is reasonable to consider annealing behavior and strain rate effects in predicting the formation of residual stress and plastic strain. Therefore, the physics-based and phenomenological plasticity models are employed in AM simulations, such as Mechanical Threshold Stress model, and Johnson-Cook model. Table 3 presents a list of mechanical models reported in AM simulations (not all the articles are referred), and obviously, more research is still required. For example, the investigations of Pu *et al.* [126] shows that joint path strategies play an important role in mechanical behavior of manufactured part.

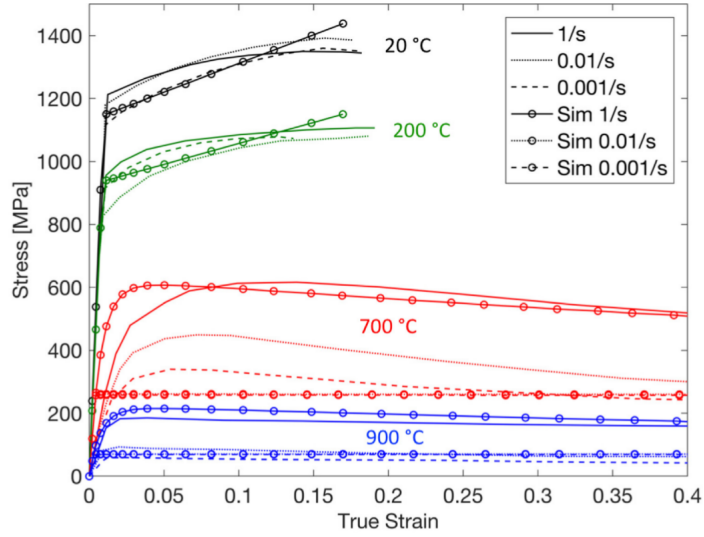


Figure 16: Comparison between experimental and simulation stress–strain response for Ti–6Al–4V at varying temperatures and strain rates, adapted from [122; 121].

Table 3: List of mechanical models used in AM simulations

Mechanical model	effects included	Reference
Thermo-elasto-plastic models with isotropic hardening	temperature softening	[42; 118; 119; 127]
Thermo-elasto-visco-plastic models with isotropic hardening	temperature softening and annealing effect	[125]
Temperature-dependent switching constitutive equations proposed by Goldak <i>et al.</i>	temperature softening, annealing behavior and strain-rate effect	[121; 128]
Mechanical Threshold Stress model	dislocation content	[129]
(Modified) Johnson-Cook (JC) plasticity models	dislocation content	[124; 130; 131]
Physically-based mixed-phase structure-property model	solutes, grain size, phase volume fraction and dislocation density	[132]

### 3.4. speed-up strategies

Even though the part-scale simulation has already made a lot simplifications, such as disregarding interactions between powder and laser/powder, fluid-dynamic in melt pool, a complete thermal-mechanical simulation with fine mesh along all the building paths will takes many hours or days [133]. To reduce the computing time, different techniques have been proposed and applied in AM simulations.

#### 3.4.1. adaptive mesh refinement

To capture the high gradient of temperature and strain during the simulation, the fine mesh is required around the heat source. Figure 17 shows two typical adaptive mesh refinement techniques (AMR) reported in literature[119; 134; 135; 136]. Figure 17-(a) is a static adaptive mesh refinement technique, which means the re-meshing is carried out after building each layer. Figure 17-(b) shows a dynamic adaptive mesh refinement technique. At beginning of each time step, a fine mesh is created in the reference frame related to heat source.

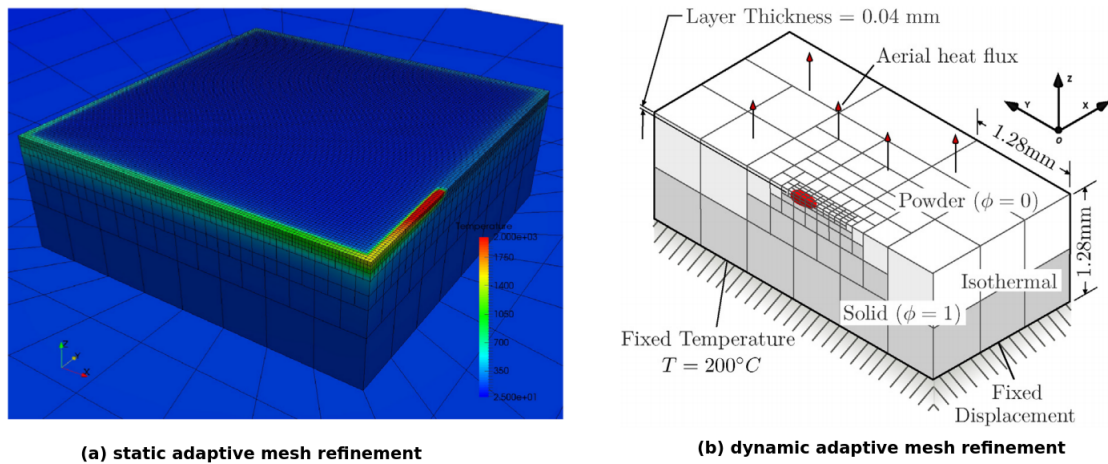


Figure 17: Adaptive mesh refinement techniques, adapted from [135; 119].

Compared to the static AMR technique, the dynamic AMR is supposed to be more efficient, as the local refinement around heat source leads to much fewer DOF than the static AMR technique. However, frequent re-meshing operations requires frequent equation renumbering, solver initialization and data transfer operation, which could also result in computational costly.

#### 3.4.2. hatch-by-hatch and layer-by-layer deposition

Simulation of a moving laser spot along the scanning path requires fine mesh to capture the high gradient of temperature and strain, and the element size highly depends on spot size. The laser spot should contain at least 4 elements to ensure a good prediction accuracy, one should note that an important gap between element size (in 10-30 micrometers) and part scale (in millimeters) exists. Moreover, small-time steps should be chosen to ensure a numerically continuous solution. All these features lead to the rise of computing time.

In order to circumvent the difficulty due to fine discretization of time and space, the hatch-by-hatch and layer-by-layer deposition techniques [137; 138; 139; 140] are employed to accelerate the AM simulations. Figure 18 presents an illustration of hatch-by-hatch and layer-by-layer deposition techniques. As laser spot is not included in the simulation, the element size could be much larger.

The thermal cycle of hot track can be obtained by two ways: (i) a single-track step-by-step heat conduction simulation [141] or a steady-state analytical solution; (ii) a representative surface or body heat flux (see figure 19) applied to a target volume (scan or layer) for an arbitrary time period [137; 140]. In case of applying a representative surface or body heat flux, the new energy density should be calibrated [138; 140] to ensure a correct fusion profile.

To enable modeling the large-sized samples at an affordable computational cost, multi-hatch-by-multi-hatch and multi-layer-by-multi-layer [137; 138] also have been used in AM simulations. Bayat *et al.* [137] has conducted an

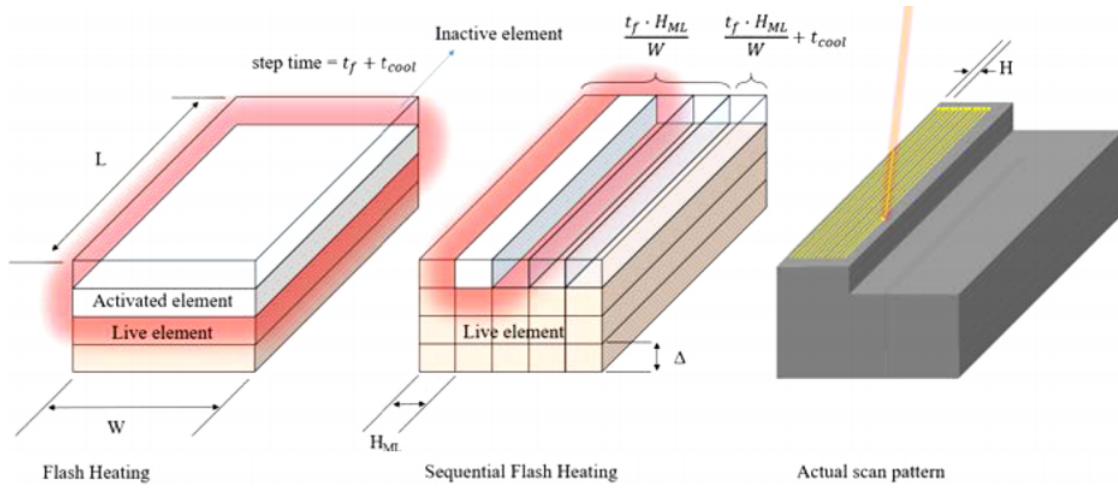


Figure 18: Schema illustration of hatch-by-hatch and layer-by-layer deposition techniques, adapted from [137].

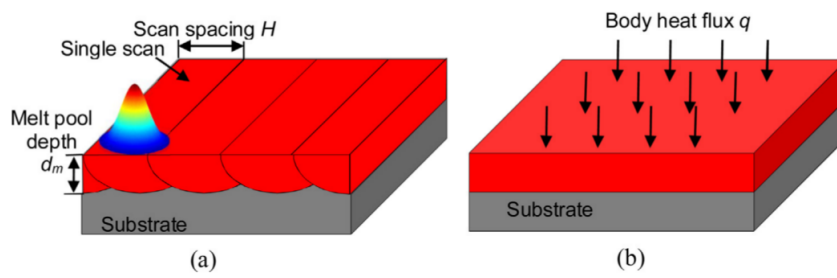


Figure 19: Modeling of body heat flux in the meso-scale layer hatch model: (a) hatch creation scan by scan, (b) hatched layer with body heat flux. [140].

investigation of the effect of activation strip width on distortion, and results presented in figure 20 shows that too large strip width leads to poor prediction in distortion.

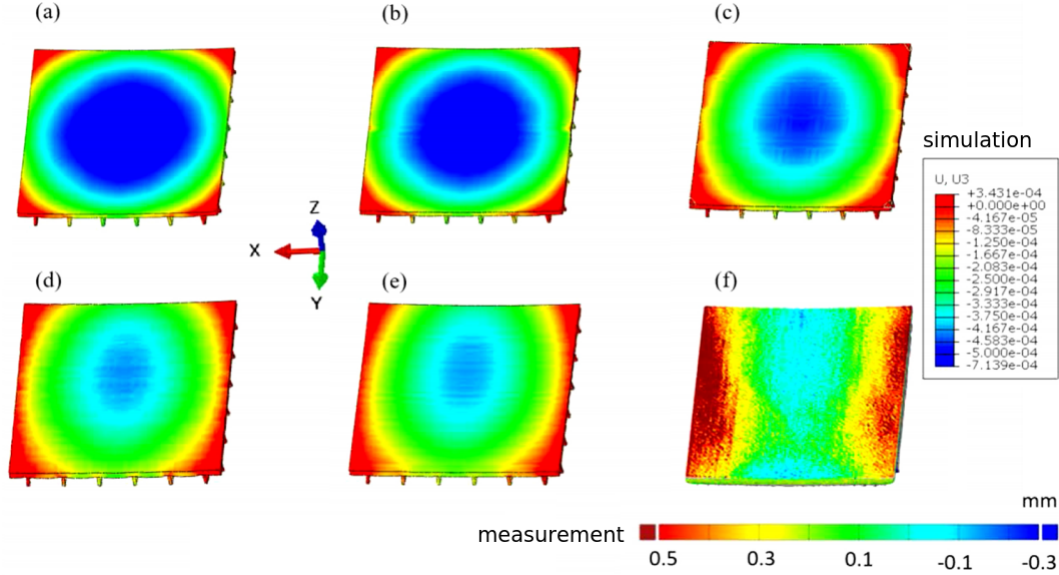


Figure 20: Final z-deflection field after the cutting process for: (a) SFH-30, (b) SFH-15, (c) SFH-06, (d) SFH-03 and (e) SFH-1.5. (f) is the actual measurements done by 3D scanning with the fringe projection technique [137].

### 3.4.3. inherent strain method

To enable simulate the bigger geometries, inherent strain method [142; 143] has also been employed to simulate AM. The inherent strain can be obtained either X-ray/neutron diffraction strain measurements [144] or the numerically computed inherent strains [145].

In experimental measurements of inherent strain procedure, the residual stress/strain will be measured at different distances near the bead. The experimental values will be used to reconstruct the inherent strain state as a function of spatial coordinates. Once the arbitrary shape functions are fitted, the experimentally estimated eigenstrains can be applied in the part-scale mechanical model for final stress/deformation prediction.

For the numerically computed inherent strains procedure, a full thermal-mechanical simulation is carried out on a sub-model (a small block). The final strain extracted from the sub-model are then applied in a part-scale elasto-plastic FE model to predict residual stresses and deformations of the real part. This work is based on the assumption that the complete part is generated by a build-up of the same sub-models. Li *et al.* [146] presents a multi-scale methodology to simulate the residual stress and distortion during SLM, as it can be noticed from figure 21. This multi-scale methodology is quiet similar to inherent strains method, and the simulation speed-up is achieved by imposing the distortion and residual stress field to part model.

The inherent strain method is computational efficient even for large and complex structures, as the inherent strain FE analysis use only the material constitutive law and properties at ambient temperature. Furthermore, the mesh size used in inherent strain method can be much bigger than the element size in step-by-step thermal-mechanical simulation.

### 3.4.4. remarks

A comparison of different strategies is shown in table 4, which can give a better insight into the accuracy, computational cost, applicability, and simulation size. The inherent strain method is not included in this comparison, since the accuracy and efficiency of the inherent strain method strongly depend on measurements or the selection of the sub-model.

1. Step-by-step simulation allows studying the effect of process parameters, such as laser speed, laser energy distribution, spot size, etc. The microstructure related to process parameters can also be investigated, and the

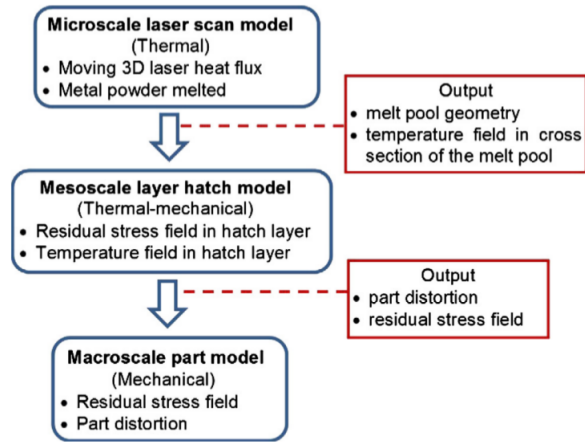


Figure 21: Multi-scale methodology for fast prediction of part distortion and residual stress [146].

Table 4: Comparison of speed-up strategies developed in FEM frame work, adapted from [138]

Strategy	Accuracy	Efficiency	Applications	Build size
Step-by-step with fine mesh	●●●●●	●○○○○○	Thermal-physical, thermo-mechanical, meso-scale, and powder-scale analyses.	few tracks and layers
Step-by-step with AMR mesh	●●●●●	●●○○○○	Thermal-physical, thermo-mechanical, meso-scale, and powder-scale analyses.	small part
Hatch-by-hatch	●●●●○	●●●○○○	Scanning path design, thermo-mechanical, part-scale.	medium part
n-hatch-by-n-hatch	●●●○○○	●●●●○○	Scanning part design, thermo-mechanical, part-scale	medium and large part
Layer-by-layer	●●○○○○	●●●●●○	Number of parts on single build, thermo-mechanical, part-scale	Large and complex geometry
n-layer-by-n-layer	●○○○○○	●●●●●●	Number of parts on single build, thermo-mechanical, part-scale	Very large and complex geometry

thermal-mechanical simulations are generally limited to a few tracks/layers ( $< 1 \text{ mm}^3$ ). Step-by-step with AMR mesh allows simulating the building of small part ( $< 10 \text{ mm}^3$ ).

2. Hatch-by-hatch technique can be used to optimize the scanning strategies. Hatch-by-hatch or n-hatch-by-n-hatch is an efficient alternative to assist in many engineering decisions, such as the orientation of the part, residual stress or strain controlling. Printing of medium part ( about  $100 \text{ mm}^3$ ) can be simulated.
3. Layer-by-layer is destined to simulate the large and complex geometry, and n-layer-by-n-layers technique is for very large building part.

Increasing efficiency is generally accompanied by reduction of accuracy (or requirements of more calibrations), therefore, the selection of speed-up strategy should adapt to the requirements. For example, we can not employ the hatch-by-hatch technique to investigate the effect of energy distribution on melt pool size since the heat source is not included in this simulation.

### 3.5. Conclusion

As shown in previous sections, the thermal-mechanical simulation of AM has been well studied. One should note that the melt pool connect the solid part and powder/laser, however, strong assumptions has been made for melt pool and thermal filed simulation. Furthermore, as the thermal results is responsible for the microstructure and mechanical consequences, more accurate numerical models and studies concerning heat transfers are required.

## 4. Meso/powder-scale multiphysics models in PBF and DED

Meso/powder-scale models focus on simulating the interactions that have been disregarded in part-scale models, and the high-fidelity meso/powder-scale models allows better appreciating the effects of process parameters. Different numerical methods have been developed and applied to modeling DED and PBF, such as FEM/FVM, level-set, and VOF, etc. Figure 22 summarize the multiphysics problems that we will discuss in this section. Compared to numerical modeling of BPF, DED involves more couplings related to the dynamic effect of powder particle. The energy input in DED and PBF is considered as laser beam for simplicity.

In order to make a clear presentation and give insight of each numerical method, this section consists of two parts: interactions of powder-related and laser-related, mass/heat transfers in melt pool and bulk, since two parts are generally performed in uncoupled manner. The modeling results of interactions of powder and laser beam will be used as the input of mass/heat transfers simulations.

### 4.1. Interactions of powder-related and laser-related in PBF

In PBF process, the powder is deposited layer by layer as it can be noticed from figure 3-(b). In the literature, there are two different ways to model the powder layer. The first approach is to treat the powder layer as a continuum medium [147; 148; 149] (see the second model in figure 4) like in part-scale FEM presented in 3.2.2, which can largely reduce the size of mesh discretization. In addition, the effective thermal-dependent material properties explained in Section 3.2.2 can also be incorporated to describe the properties of the powder layer. Similar to heat conduction simulations, a 2D or 3D heat source (Table 1) is generally employed to simulated the effect due to irradiation and ray propagation. The second approach consists of considering the realistic geometry of powder particles [74; 150; 151; 152]. The powder layer can be constructed with a uniform particle size and orderly packing [150], or powder spreading model using the Discrete Element Method (DEM) [74; 152; 153], and advantage of DEM method allows taking realistic packing conditions (interactions between powder and powder/substrate) into consideration.

The particle movement in DEM is in Lagrangian description, and its governing equations of linear and angular momentum are

$$\begin{aligned}
 m_p \frac{dv_p}{dt} &= \mathbf{F}_f + \mathbf{F}_D + \mathbf{G}_i + \Sigma \mathbf{F}_{p-p} + \Sigma \mathbf{F}_{p-s}, \\
 I_p \frac{dw}{dt} &= \Sigma \mathbf{M}_t + \mathbf{M}_r \\
 \text{with} \quad \mathbf{F}_f &= -V_p \nabla p
 \end{aligned} \tag{14}$$

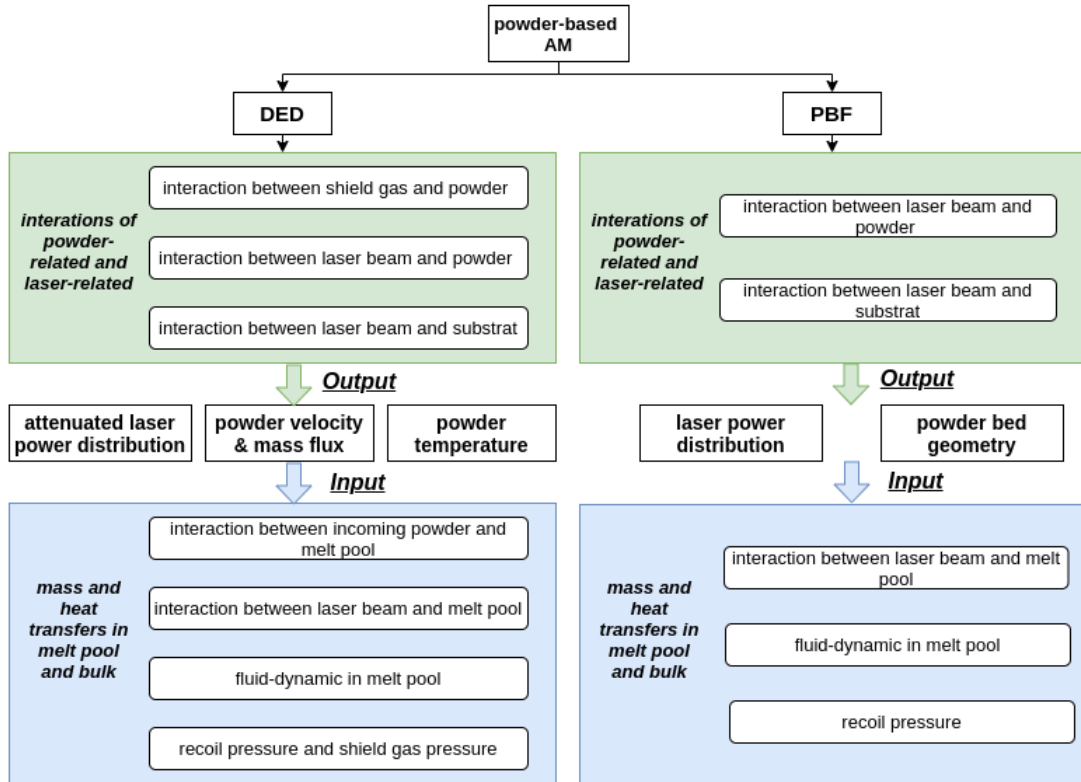


Figure 22: multiphysics modeling in DED and PBF.

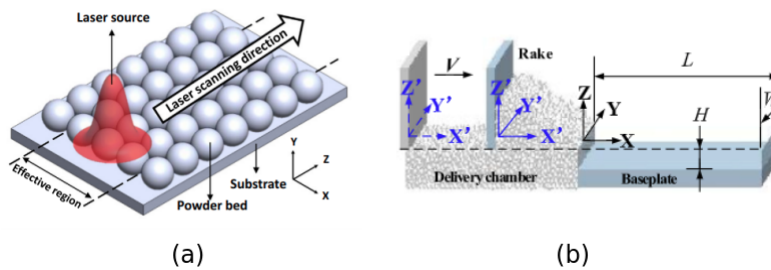


Figure 23: Example of powder particle deposition; orderly packing (a) and powder spreading model (b), adapted from [150; 153].



where  $m_p$ ,  $v_p$ ,  $V_p$ ,  $I_p$  are the mass, velocity, volume, rotational inertia of particle;  $F_f$ ,  $F_{DM}$  represent buoyancy force, gravity force respectively;  $G_i$  is the force of gravity in  $i$  direction;  $p$  is the ambient pressure of an inert gas.  $F_{p-p}$  and  $F_{p-s}$  stands for particle-particle and particle-substrate interaction force.  $\omega$  is the angular velocity;  $M_t$ ,  $M_r$  are the moment generated by tangential forces of interaction force and rolling friction torque. Relevant details can be found in [152; 154; 155; 156].

After the deposition of powder layer, ray-tracing techniques [84; 148; 157] have been used to calculate real energy distribution. As it can be noticed from figure 24, a sufficient number of rays replace the continuous Gaussian beam. Every ray is traced in an explicit manner until it is totally absorbed or reflected outside the powder bed. However, the ray-tracing simulation is extremely time-consuming; for simplicity, a 3D volume heat source can be calibrated through the absorbed energy intensity given by the ray-tracing technique.

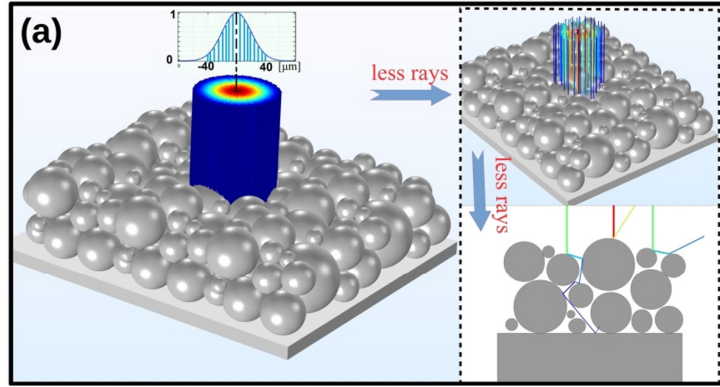


Figure 24: Powder-substrate geometry, laser beam and ray tracing, adapted from [148].

#### 4.2. Mass/heat transfer in melt pool and bulk in PBF

The Lattice Boltzmann method (LBM), Smoothed Particle Hydrodynamics (SPH), finite element method (FEM) and finite volume method (FVM) are main ways reported in the literature to model mass and heat transfers in melt pool. In general, the finite element method will only model metallic material (solid or liquid), and the volume of gas is disregarded. The finite volume method consist of modeling two-phase flow (gas and solid or liquid); thus, special algorithm is required to capture free interface between gas and metallic material. We start with governing equations targeting modeling melt-pool :

$$\begin{aligned}
 \text{Mass Conservation :} & \quad \frac{\partial \rho}{\partial t} + \nabla \cdot (\rho \mathbf{v}) = 0 \\
 \text{Momentum Conservation :} & \quad \frac{\partial (\rho \mathbf{v})}{\partial t} + \nabla \cdot (\rho \mathbf{v} \otimes \mathbf{v}) = -\nabla \cdot p + \nabla \cdot \boldsymbol{\tau} + \mathbf{S}_{mom} \\
 \text{Energy Conservation :} & \quad \frac{\partial (\rho C T)}{\partial t} + \nabla \cdot (\rho C T \mathbf{v}) = \nabla \cdot (k \nabla T) + S_{energy}
 \end{aligned} \tag{15}$$

where  $\mathbf{v}$ ,  $p$ ,  $\boldsymbol{\tau}$  are velocity, hydrostatic pressure and the deviator of the tensor of the constraints of Cauchy.  $\mathbf{S}_{mom}$  is the sources termes for momentum, such as buoyancy force, gravity force, or surface tension;  $S_{energy}$  represents the sources term of energy, such as laser irradiation, convection and radiation losses.

Körner *et al.* employed the Lattice Boltzmann Method [74; 158] to investigate the balling effect, and wetting phenomena numerically. They also reported that the packing density has significant effect on melt pool characteristics such as balling. However, LBM has been reported [159] that there are numerous limitations for modeling laser melting processes. For example, the need for a fine lattice-mesh to accurately capture the mesh motion as well as an unclear methodology for modeling some of the thermal effects in the energy equation.

In the FEM method, the domain of material should be discretized by the elements. However, considering realistic geometry of powder particles in 3D would lead to a heavily meshing task, sometimes even become impossible. Certainly, re-meshing procedure is sometime required to avoid mesh tangling. ALE3D [27; 151; 160] has been applied

to carry out such simulations in 3D. For simplifying the mesh operations, Tseng *et al.* [150] employed the 2D model to investigate the interfacial dynamics. To completely circumvent heavily meshing operations, the continuum medium method presented in 4.1 is much more friendly for meshing, which has been widely used in modeling PBF [161]. Since the mesh-based FEM is sometimes constrained by re-meshing, the free mesh method like SPH seems an optimal solution for modeling heat and mass transfers in melt pool. Several efforts have been made to model AM process. Trautmann *et al.* [162] developed a three-dimensional multiphysics SPH model to simulate molten pool flow, where the effects of gravity, buoyancy, as well as surface tension forces and dynamic viscosity are considered. Russell *et al.* [161] adapted the SPH method to resolve thermal, mechanical, and material fields in a laser-based AM process involving heating (including thermal expansion), melting, as well as re-solidification of metallic materials were simulated. Further numerical simulations of the 3D PBF process by SPH were carried out [163; 164; 165]. They investigated the relationship between the different processing parameters and the morphology of molten pool. Multi-Resolution SPH [166], FEM-SPH coupling method [167], GPU-accelerated 3D SPH model [168] have also been developed to reduce the computational effort.

To model the molten pool using FVM, the interface between gas and solid/liquid must be tracked with appropriate boundary conditions. Volume of fluid (VOF) [169] method gains intensive attentions and utilization thanks to open source codes (*OpenFOAM*), which employs a set of fixed rectangle or hexahedral grids in space. The conservation equation of fluid fraction is calculated:

$$\frac{\partial \chi}{\partial t} + \frac{\partial (v_i \chi)}{\partial x_i} = 0 \quad (16)$$

with  $\chi$  the base material fraction. Specifically,  $\chi = 0$  indicates a void cell where only gas is present,  $0 < \chi < 1$  refers to an interface cell containing both gas and base material,  $\chi = 1$  depicts a cell completely occupied by base material. The VOF equation should be solved systematically together with equation 15. In case of presenting mixture of two phase in one cell, the thermophysical properties are weighted by the volume fraction and described as:

$$\phi = \phi_1 \chi + \phi_2 (1 - \chi) \quad (17)$$

where  $\phi$  could be some generic material properties, such as density, heat capacity, dynamic viscosity and thermal conductivity; subscript 1,2 are the base material and gas. More details can be found in [152; 170].

The level-set (LS) method is another widely used interface tracking approach in finite element/volume approach [149], by applying a level-set function to calculate the interface region [171]. In general, the zero-level set represents the interface of gas/material, and other levels sets are symmetrical positioned at various distances from the interface [172]. The level set function  $\psi(\mathbf{x}, t)$  is advected through the integration of an advection equation:

$$\frac{\partial \psi}{\partial t} + \mathbf{v} \cdot \nabla \psi = 0 \quad (18)$$

The advective flow field  $\mathbf{v}$  in equation 18 is the velocity solution calculated from Navier–Stokes equations. Actually, only the normal component of  $\mathbf{v}$  is needed to update interface:  $v_N = \mathbf{v} \cdot \frac{\nabla \psi}{|\nabla \psi|}$ ; therefore, equation 18 can written as

$$\frac{\partial \psi}{\partial t} + v_N |\nabla \psi| = 0 \quad (19)$$

One of possible formulation is to set the level set function to be positive and negative in the base material phase and gas phase, respectively:

$$\psi(\mathbf{x}, t) \begin{cases} > 0 & \text{if } \mathbf{x} \in \text{base material phase} \\ = 0 & \text{if } \mathbf{x} \in \Gamma \\ < 0 & \text{if } \mathbf{x} \in \text{gas phase} \end{cases} \quad (20)$$

To avoid the sharply change of properties at interface, a smoothed Heaviside functions  $H(\psi)$  is introduced to create a transition zone around the interface ( $\psi = 0$ ).  $H(\psi)$  varies from 0 to 1 within a total thickness  $2l$  and keeps constant outside [149]:

$$\mathcal{H}(\psi) = \begin{cases} 0 & \psi < -l \\ \frac{1}{2} \left[ 1 + \frac{\psi}{l} + \frac{1}{\pi} \sin\left(\frac{\pi\psi}{l}\right) \right] & |\psi| \leq l \\ 1 & \psi > l \end{cases} \quad (21)$$

Apart from tracking interface of L/G and L/S, the following continuum model [173; 174] is commonly employed to make the transport equation valid for the entire computation domain (gas, liquid and solid), and physical properties of transient layer are smoothed as follows:

$$\begin{aligned} \rho &= \begin{cases} (1-H)\rho_l + H\rho_g & L/G \\ f_s\rho_s + f_l\rho_l & L/S \end{cases} \\ h &= \begin{cases} (1-H)h_l + Hh_g & L/G \\ f_s h_s + f_l h_l & L/S \end{cases} \\ k &= \begin{cases} (1-H)k_l + Hk_g & L/G \\ \left(\frac{f_s}{k_s} + \frac{f_l}{k_l}\right)^{-1} & L/S \end{cases} \\ \mu &= \begin{cases} (1-H)\mu_l + H\mu_g & L/G \\ \mu_l \frac{\rho_s}{\rho_l} & L/S \end{cases} \end{aligned} \quad (22)$$

where  $\rho$ ,  $h$ ,  $k$ ,  $\mu$  are the properties of density, enthalpy, thermal conductivity and viscosity. The subscript  $s$ ,  $l$ ,  $g$  represent solid, liquid and gas.  $H$  is the Heaviside functions in equation 21.  $f_s$  and  $f_l$  are the volume fraction of liquid and solid, respectively, which are expressed as :

$$\begin{aligned} f_s &= 1 - \frac{F_l}{\rho_l} \left( \frac{1-F_l}{\rho_s} + \frac{F_l}{\rho_l} \right) \\ f_l &= \frac{F_l}{\rho_l} \left( \frac{1-F_l}{\rho_s} + \frac{F_l}{\rho_l} \right)^{-1} \end{aligned} \quad (23)$$

The mass fraction at the solid/liquid interface can be calculated by using temperature :

$$F_l = \begin{cases} 0 & \text{for } T < T_s \\ \frac{T - T_s}{T_l - T_s} & \text{for } T_s \leq T \leq T_l \\ 1 & \text{for } T > T_l \end{cases} \quad (24)$$

$$F_s = 1 - F_l$$

Figure 25 illustrate difference between VOF method and level-set method in finite volume approach. The VOF first calculate the volume fraction of base material, and the continuum surface force technique [175] is adopted to construct a continuum interface. The level-set method will use the  $v_N$  computed from N-S equations to update the L/G interface.

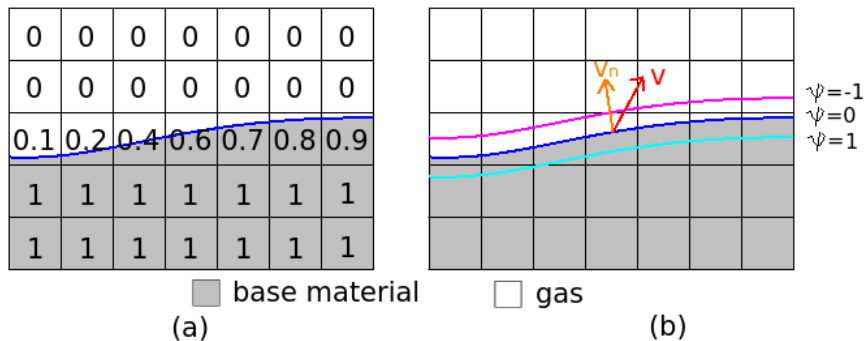


Figure 25: Schema illustration of VOF (a) and level-set method (b).

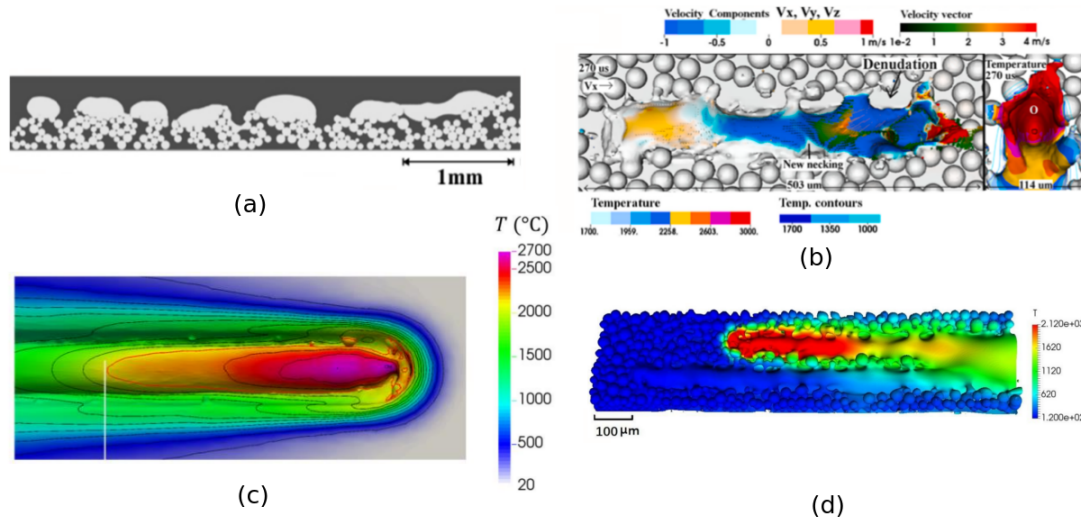


Figure 26: Molten pool simulated by aforementioned models: Lattice-Boltzmann model [74] (a), ALE3D [151] (b), In-house LS-FEM code [149] (c), OpenFOAM [152] (d).

Figure 26 shows some simulations results given by aforementioned models. LBM simulations in 2D presented by Körner *et al.* [74; 158] give insights of the importance of powder packing. However, there is no software or open-source code is available in 3D LBM, Moreover, Khairallah *et al.* [151] reported that LBM suffers severe numerical instabilities when accounting for the temperature. ALE3D developed by Lawrence Livermore National Laboratory address 2D and 3D multiphysics engineering problems using a hybrid finite element and finite volume formulation on an unstructured grid. ALE3D can investigate not only the fluid dynamic in molten pool but also different kinds of pore defect formation (depression collapse, lateral pores, open and trapped pores) [151]. Simulation result in Figure 26-(c) is given by a FEM with a level set formulation [149], this model allows investigating the effect of process parameters on stability and regularity of the solidified track. Since the realistic powder geometry is disregarded, the powder-related parameters cannot be elucidated directly in numerical model, such as packing, powder size distribution. Open-FOAM has been widely used to investigate the process parameters, to which phenomena such as balling effect, vaporization, and track irregularity were connected. Figure 5 summarizes some majors multiphysics models presented in the literature.

Table 5: Summarize of some major multiphysics models in modeling PBF

Strategy	Software (reference)	Physics
Continuum medium + FEM	Comsol multiphysics [176]	(a-c),(f),(g)
Continuum medium + FEM	In-house LS-FEM code [149; 177]	(a-d),(f),(g),(i)
DEM + LBM	In-house LBM code [166], Dual-SPHysics [168]	(a-h)
SPH	In-house SPH code [74; 158]	(a-h)
Powder packing + FEM/FVM	ALE3D [27; 151; 160]	(a-g)
DEM + FVM	CFDEM [152] + Open-FOAM [178; 179; 180; 181]	(a-i)
DEM + FVM	DEM + Flow-3D [182; 183; 184; 185]	(a-i)
DEM + FVM	ESL_ACE+ [186; 187; 188; 189]	(a-i)

(a) Marangoni effect; (b) Buoyancy effect (c) Surface tension; (d) Densification; (e) Realistic powder geometry; (f) Recoil pressure; (g) Vaporisation; (h) powder-related interactions; (i) laser-related interactions;

### 4.3. interactions of powder-related and laser-related in DED

In the DED process, interaction between the powder stream and laser beam alters the temperature of powder particle and energy distribution and intensity of laser beam reaching the deposition melt pool, which would significantly affect the melt pool and deposition tracks [190]. Furthermore, the thermal field is highly responsible to residual strain/stress and microstructure of final part. To better understand the effect of process parameters, both experimental and numerical studies have been carried out [190; 191; 192; 193]. As the temperature of powder and intensity of laser at consolidation plane are two main input parameters for mass/heat transfers simulation, the numerical methods and models focus on modeling interactions will be presented.

Table 6 review typical methods used in modeling the interactions. The analytical method considers only the interaction between powder and laser, and powder concentration and movement are generally pre-defined. The one-way coupling method will calculate the gas turbulent flow without considering the impacts of powder particles on gas flow, while the effect of gas flow on powder particle will be taken into account. The two-way coupling method computes the gas flow and the movement of powder particles in a strong coupling manner. The equilibrium of powder particles and gas flow are solved together.

Table 6: Typical numerical methods applied in modeling interactions in DED

Numerical method	interaction(s) into account
Analytical method [194; 195]	interaction between powder and laser
one-way coupling method [196; 197]	impacts of gas flow on powder particle
	interaction between powder and laser
	(optional) collisions among particles
	(optional) interaction between gas flow and substrate (pre-deposited layers)
two-way coupling method [198; 199; 200]	strong coupling between powder and gas
	interaction between powder and laser
	(optional) collisions among particles
	(optional) interaction between gas field and substrate (pre-deposited layers)

#### 4.3.1. analytical method

Figure 27 presents the steps and orders followed in analytical modeling. The first step is to determine the powder flux distribution below the exit of nozzles, and the effects of carrier gas on powder distribution are disregarded. Once the powder distribution is determined, the total powder mass within the laser beam can be calculated. Step two is to statically analyze the laser attenuation due to the powder particles within the laser beam, which allows determining quantitatively the laser energy distribution below the nozzle. Calculation of powder particle heating is the last step, since the laser attenuation and trajectory of powder particle are required to calculate the irradiation of laser. One should note that the selected function to describe powder flux distribution is crucial to the prediction of laser attenuation and particle heating. Two examples are presented in following sections.

The analytical models are computational efficient, and assumptions are made to establish the relationship between process parameters and output results (temperature of powder and attenuation of laser). The assumptions can be

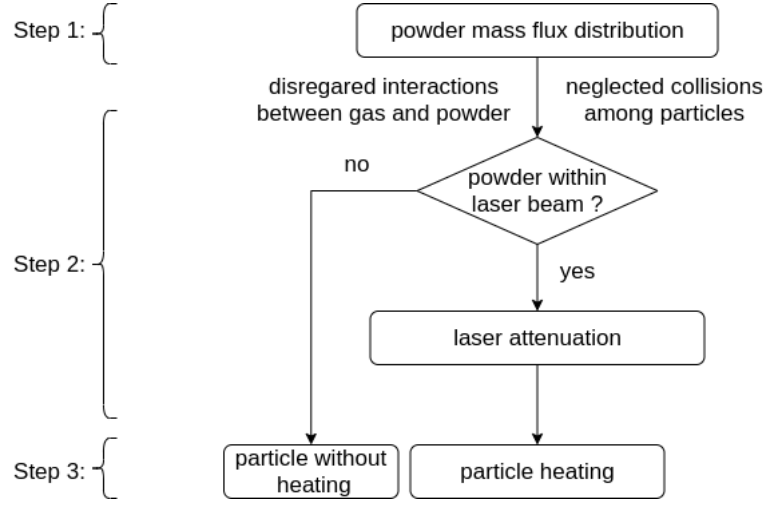


Figure 27: Workflow of analytical modeling.

summarized as [194]:

1. The particles are assumed to be spherical and identical with the average radius [191; 194; 201]. Because of low volume fraction of powder particles, the collisions of particles are neglected.
2. The powder stream and gas flow are treated as steady state with constant velocity. The effect of gravity and drag force are negligible [191; 202], since the interaction time is too short for the particles to cross the beam-powder interaction zone.
3. The temperature of particles are solved by treating the particles as lumped capacity volume because of low the Biot number [202; 203]. Convective and radiative losses in the stream are faible and neglected.
4. Laser attenuation is often proportional to the area of the particles projected to the beam [204; 205], and particle heating due to reflected energy may be negligible [203; 196].
5. At any cross-section, the powder flow follows Gaussian distribution or addition of multiple Gaussian distribution, which has been confirmed by the experimental results [193; 206].

According to the nozzle type used in DED, there are three types of nozzles including coaxial nozzle, three-jet nozzle, and four-jet nozzle, and figure 28 presents two typical nozzles. Two analytical models proposed in the literature will be demonstrated.

Liu *et al* [191] has proposed analytical modeling and experimental validation of powder stream distribution for four-jet nozzle. The similar idea as Pinkerton is adopted, and the powder flux rate distribution below the nozzle is supposed to be Gaussian. Figure 29 shows an diagram of powder stream, and the powder flux distribution at a point  $P(r, z)$  before the converging point can be expressed as:

$$\begin{aligned}
 M(r, z) &= M_A + M_B + M_C + M_D \\
 &= \frac{m}{\pi r_s^2} \left[ \exp\left(\frac{-2a^2}{r_s^2}\right) + \exp\left(\frac{-2b^2}{r_s^2}\right) + \exp\left(\frac{-2c^2}{r_s^2}\right) + \exp\left(\frac{-2d^2}{r_s^2}\right) \right] \\
 &\text{where} \\
 a &= \left| \left( \frac{d_c - z}{d_c} \right) d_p - r \right| \\
 b &= \left| \left( \frac{d_c - z}{d_c} \right) d_p + r \right| \\
 c &= d = \sqrt{r^2 + (r + a)^2}
 \end{aligned} \tag{25}$$

where  $r_s$  is the powder stream radius that is written as  $r_s = \frac{z}{d_c}(L - r_0 + r_0)$ .

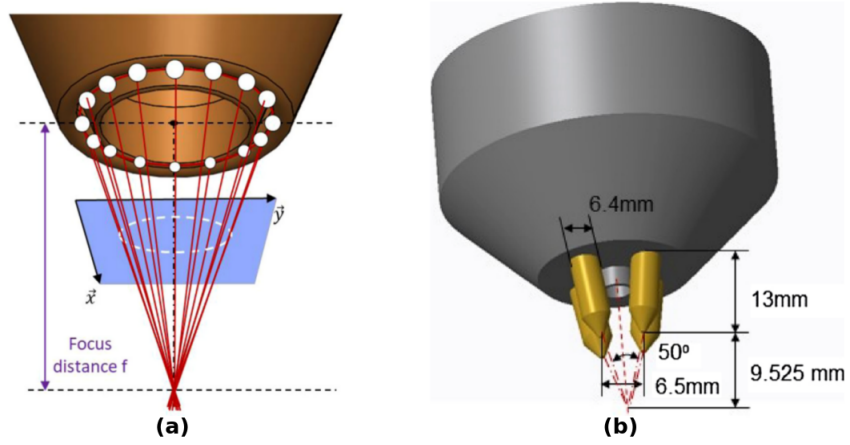


Figure 28: Example of nozzle type: coaxial nozzle (a) and four-jet nozzle (b), adapted from [191; 193].

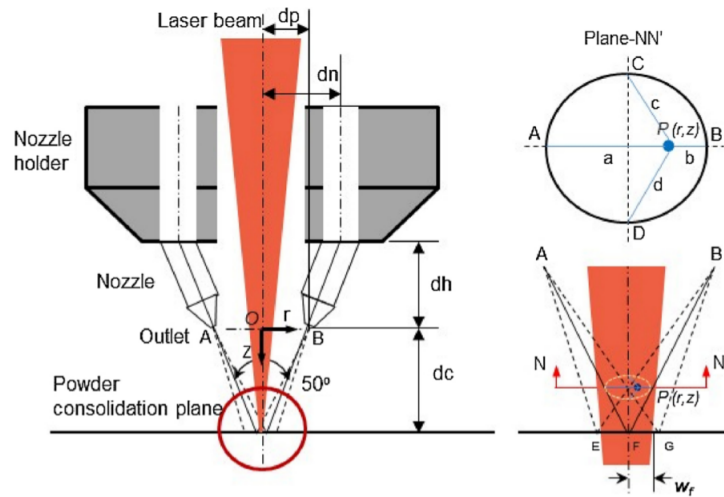


Figure 29: Schematic diagram of the powder stream from a four-jet deposition nozzle, adapted from [191].

Pinkerton [190] has proposed an analytical model to determine the laser attenuation, powder flux and particle heating during DED process, and this model has been widely accepted and used [207; 208; 209; 210; 211]. The coaxial nozzle has been simplified as a 2D axisymmetrical problem, as it can be noticed in figure 30 and some geometrical parameters are also shown. The powder distributions and powder temperature predicted have been verified and validated by experimental results.

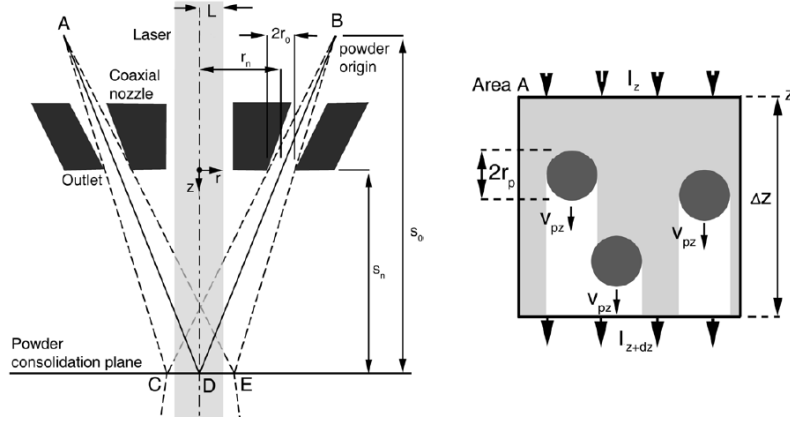


Figure 30: Schematic diagram of the powder stream from a coaxial laser deposition nozzle (a) and Schematic diagram of beam attenuation by the powder at any position where they interact (b), adapted from [190].

At any position \$(z,r)\$ for \$0 < z < s\_n\$ and \$r > 0\$, we have:

$$\begin{aligned}
 \text{powder distribution: } P &= \frac{1}{2} \left[ \frac{2m}{\pi r_s^2} \exp\left(-\frac{2a^2}{r_s^2}\right) \right] + \frac{1}{2} \left[ \frac{2m}{\pi r_s^2} \exp\left(-\frac{2b^2}{r_s^2}\right) \right] \\
 \text{with } a &= \left| \left( \frac{s_n - z}{s_n} \right) r_n - r \right|, \quad b = \left| \left( \frac{s_n - z}{s_n} \right) r_n + r \right| \quad \text{and } r_s = r_0 + \frac{zr_0}{s_0 - s_n} \\
 \text{laser attenuation: } I(z, r) &= I(0, r) \left( 1 - \frac{3}{4v_{pz}r_p\rho} \int_0^z P_r(z) dz \right) \\
 \text{energy balance for heating powder: } \alpha I(z, r) \pi r_p^2 \frac{\Delta z}{v_{pz}} &= \frac{4\pi r_p^3}{3} \rho c \Delta T
 \end{aligned} \tag{26}$$

where \$I(0, r)\$ is the beam intensity at \$(0,r)\$, and \$v\_{pz}\$ is powder velocity component in \$z\$ direction. \$P\_r(z)\$ corresponds the powder flux falling within the beam (\$0 < z < s\_n\$ & \$r < L\$). \$\rho\$ is the powder density. The powder flux \$P\$ comprise the powder from \$A\$ and \$B\$. \$\alpha\$ is the absorptivity of the particles to the laser radiation. \$\Delta z\$ corresponds the discretization of laser beam in \$z\$ direction as it can be noticed from figure 30.

Frenk *et al.* [212] and Huang *et al.* [202] applied Mie and Lambert-Beer theorem to describe attenuation of laser. The similar linear relationship between the laser attenuation and projected area of powders within beam has been found, and this type of model has been extensively used in the literature due to its simplicity and efficiency [213]. The mathematical formulation of laser attenuation based on Mie's theory is written as follow [212]:

$$I(z, r) = I(0, r) \left[ 1 - \exp\left(-\sigma_{ext} N_p l\right) \right] \tag{27}$$

where \$\sigma\_{ext}\$ and \$N\_p\$ are the extinction coefficient and powder concentration. \$l\$ is the the traveling distance of laser beam. Moreover, to determine the particle temperature in a realistic way, Huang *et al.* [202] not only considered the convection and radiation losses, but also treated the latent heat by using the temperature correction method. The energy balance for



heating powder presented in equation 26 becomes:

$$\frac{4\pi r_p^3}{3}\rho C\Delta T = \alpha I(z, r)\pi r_p^2 \frac{\Delta z}{v_{pz}} - \sigma\epsilon(T^4 - T_0^4)\pi r_p^2 - h_{conv}(T - T_0)\pi r_p^2$$

$$C\Delta T = \begin{cases} C_{powder}\Delta T; & \text{for } T < T_{solidus} \\ C_{powder}\Delta T + L \frac{(T - T_{solidus})}{(T_{liquidus} - T_{solidus})}; & \text{for } T_{solidus} < T < T_{liquidus} \\ C_{powder}\Delta T + L; & \text{for } T > T_{liquidus} \end{cases} \quad (28)$$

As it can be noticed from the above discussion, analytical models can make fast estimations based on several assumptions. The analytical models allow investigating nozzle design, some powder-related and laser-related process parameters, and providing input data for mass/heat transfer modeling. However, the some over-simplified assumptions related to powder particle (shape and size) and its interactions with gas could also reduce the precision of predictions. Numerical methods though computational fluid dynamics techniques can give better predictions by considering more complex multiphysics couplings but these methods could be more time-consuming.

#### 4.3.2. one-way and two-way coupling method

Since analytical method disregarded the several interactions and particle trajectory is calculated with pre-defined movement, the numerical models aims to make high-fidelity modelings. Two-phase turbulent flow, including continuum phase of gas and powder particles, can be modeled by computational fluid dynamic (CFD) techniques. Figure 31 shows a resume of the workflow of one-way and two-ways coupling methods as well as the governing equations, and the principle difference between one-way and two-way coupling is whether the feedback of particle on gas flow is considering. In both cases, the collision between the particles are generally ignored as a result of low volume fraction of powders.

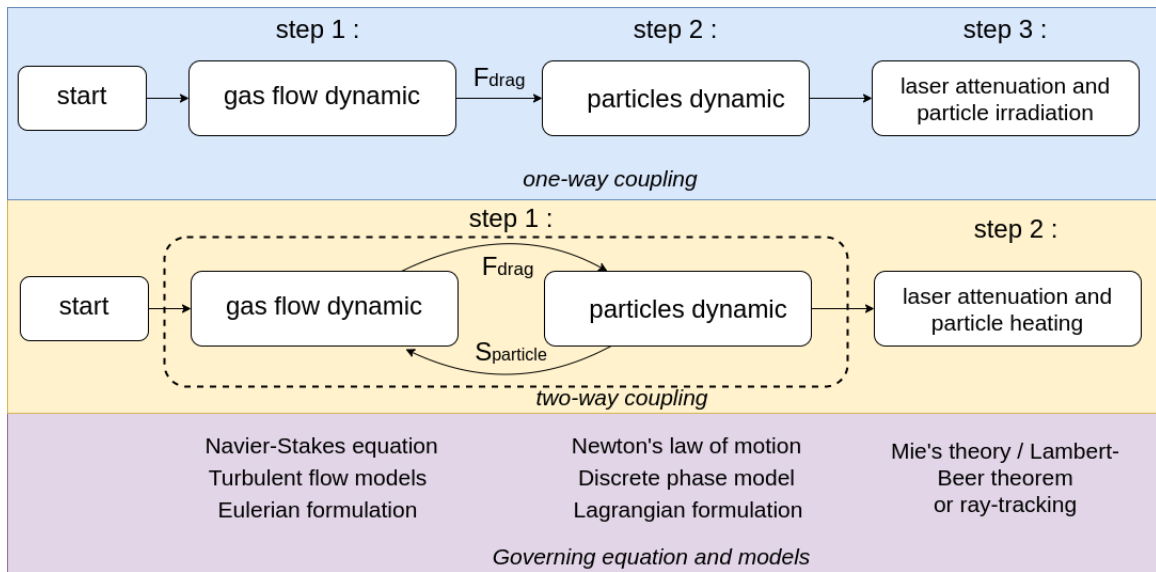


Figure 31: Resume of one-way and two-way coupling methods.

The governing equations of gas flow are modelled by Navier-Stokes equations, and the temperature change of gas flow is disregarded because of negligible variance.

Conservation of mass:

$$\frac{\partial \rho_g}{\partial t} + \nabla \cdot (\rho_g \mathbf{v}) = 0 \quad (29)$$

Conservation of momentum:

$$\frac{\partial(\rho_g \mathbf{v})}{\partial t} + \nabla \cdot (\rho_g \mathbf{v} \otimes \mathbf{v}) = -\nabla \cdot p + \nabla \cdot \boldsymbol{\tau} + \rho_g g_i + \mathbf{S}_{particle}$$

where  $\rho_g$ ,  $t$ ,  $\mathbf{v}$  are the density, time and velocity vector respectively;  $p$ ,  $g_i$  are the pressure and gravity vector;  $\mathbf{S}_{particle}$  is the source term to represent the forces exerted by powders, which is neglected in the one-way coupling method. This momentum source is computed based on the trajectories of powder particles and momentum conservation, which has been detailed in [198; 199; 200]. Then, the Reynolds Averaged Navier-Stokes approach is generally applied to model turbulent flow, by using  $k - \epsilon$  [214] or  $k - \omega$  [215] model. Furthermore, more assumptions can be made to simplify equation 29. For example, flow gas can be treated as in-compressible due to small pressure drop and low Mach number [199].

Discrete phase model (DPM) has been used extensively to model the powder dynamic, and the trajectory of phase particle is solved by calculating force balance in a Lagrangian description. To reduce the computational cost, a package of powder particles will be regarded as a continuum volume, and its governing equations follow Newton's laws of motion.

$$\begin{aligned} \frac{d\mathbf{x}_p}{dt} &= \mathbf{v}_p \\ \frac{d\mathbf{v}_p}{dt} &= \mathbf{F}_D + \frac{g_i(\rho_p - \rho_g)}{\rho_p} \end{aligned} \quad (30)$$

where  $\mathbf{F}_D$ ,  $\frac{g_i(\rho_p - \rho_g)}{\rho_p}$  are the drag force per unit particle mass and body force due to gravity, respectively;  $\mathbf{x}_p$  is the position vector of phase particle. And the drag force can be written as:

$$\mathbf{F}_D = \frac{3\mu C_D Re}{4\rho_p d_p^2} (\mathbf{v}_g - \mathbf{v}_p) \quad (31)$$

with  $C_D$  is the drag coefficient, which depends on the shape of particle. Both spherical and non-spherical drag coefficient models have been carried out in detail analysis by Levenspiel *et al.* [216] and He *et al.* [217].

Modeling of particle heating due to laser irradiation and laser attenuation is in the last step. The governing equations of particle heating are taken the same forme as described in analytical model. Mie's and Lambert-Beer theorem have been widely used for calculating laser attenuation in the literature, while solving radiation transport equation or even Maxwell's equations are generally computationally expensive. Therefore, the idea proposed by Pinkerton [190], which consists of establishing a linear relation between the projected area of particles and its attenuation, was well suited because of its simplicity [200]. The ray-tracing method [205] is based on the similar idea.

#### 4.4. mass/heat transfers in melt pool and bulk in DED

The molten pool connects the powder stream, laser irradiation, mass addition, and heat transfer in DED. According to whether the realistic powder particles are modelled in molten pool models, the numerical models are classified into two groups: (i) molten pool models without powder stream simulation; (ii) molten pool models with powder feeding simulation.

##### 4.4.1. molten pool models without powder stream simulation

Since the powder stream is not included in molten pool models, the mass flux, laser attenuation, and heat flux are first calculated from the models presented in Section 4.3, and then fed to molten pool models. Both mass and heat flux can be imposed as boundary conditions in FEM and FVM. In the section 4.4.1, we will first present the method FEM based

on Arbitrary Lagrangian-Eulerian (ALE), which models only the metal state. The second type of method that we will revise is FVM based on VOF and Level-set, which consist of modeling gas and metal.

In general, the FEM consists of solving equation 15 only in solid and liquid material, and the modeling of gas flow is disregarded. Therefore, the boundary of mesh represents the surface of substrate or deposited layer, and an ALE moving mesh technique is frequently applied to describe the evolution of geometry due to mass addition. Morville *et al.* and Ya *et al.* [218; 219] presented 2D modeling of clad geometry and thermal results with Comsol multiphysics® software, while two different strategies have been adopted to geometry of deposited tracks.

Morville *et al.* [218] defined a moving energy distribution (uniform) and mass distribution (Gaussian) in space, and laser attenuation was not accounted in their model. The heat loss in the out of plane dimension is modeled by adding a volume sink term in energy conservation equation (equation 15), and the moving mesh is controlled by following equations :

$$v_n = \mathbf{u} \cdot \mathbf{n} + \mathbf{v}_p \cdot \mathbf{n}$$

$$\text{with } \mathbf{v}_p = N_p \frac{\eta_p m}{\rho_p \pi r_p^2} \exp(-N_p \frac{r^2}{r_p^2}) \cdot \mathbf{j} \quad (32)$$

where  $u$ ,  $v_p$  is the velocity field calculated from N-S equation and mass addition.  $N_p$  and  $r_p$  are respectively the constriction coefficient and the standard deviation of the Gaussian distribution, which are determined from experimental measurements.  $\eta_p$  represents powder catchment efficiency that is calculated by assessing the mass difference between powder delivered and deposited material, and  $m$  is powder deposition rate by the nozzles ( $g \cdot \text{min}^{-1}$ ).  $v_p$  is supposed to be 0 when the surface is not melting.  $\mathbf{j}$  is unit vector in the mesh moving direction.

Ya *et al.* [219] used the parabolic function to approximate the geometry of deposited tracks in 2D, and the parabolic shape has been validated by Onwubolu *et al.* [220] and Nenadl *et al.* [221]. A function  $F_n(y, z, t)$  is introduced to represent the geometry of deposited tracks  $n$ , as is shown in figure 32. The moving boundary due to powder addition is the derivative of the  $F_n(y, z, t)$  over time. The parameters of  $F_n(y, z, t)$  can be calibrated from experimental results.

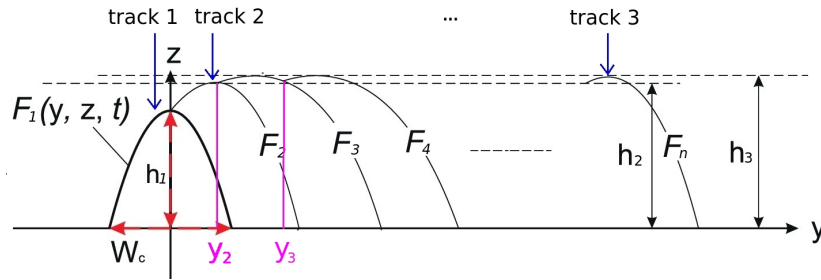


Figure 32: Schematic presentation of relationship in multi-tracks deposition, adapted from [219].

$$F_1 = a_1 y^2 + b_1 y + c_1$$

$$\text{with } F_1\left(\frac{-W_c}{2}\right) = 0, F_1\left(\frac{W_c}{2}\right) = 0, F_1(0) = h_1$$

$$F_n = a_n y^2 + b_n y + c_n$$

$$\text{with } F_n(y_n) = F_{n-1}(y_{n-1}), F_n(y_n + W_c) = 0, A_{cn} = A_{c1}$$

$$y_n = y_{n-1}, n = 2, 3, \dots \quad (33)$$

where  $n$  is the number of track.  $a_n$ ,  $b_n$ ,  $c_n$  are the parameters used to define the geometry of tracks  $n$ , and mass balance assumption is employed.  $y_n$  represent the position where the interaction appear between two successive tracks, which is calculated from  $y_n = (n - 1) \left( W_c - W_c * \frac{W_c - D_r}{W_c} \right)$  ( $D_r$  is the lateral displacement between successive tracks).

Figure 33 shows the numerical results given by ALE moving mesh technique in 2D, the thermal effect in the out-of-plane direction is modeled via a volumetric source term in energy equation [218] to match the experimental configuration; otherwise, the laser absorptivity should be calibrated with experiments [219] to obtain a good melt pool morphology.

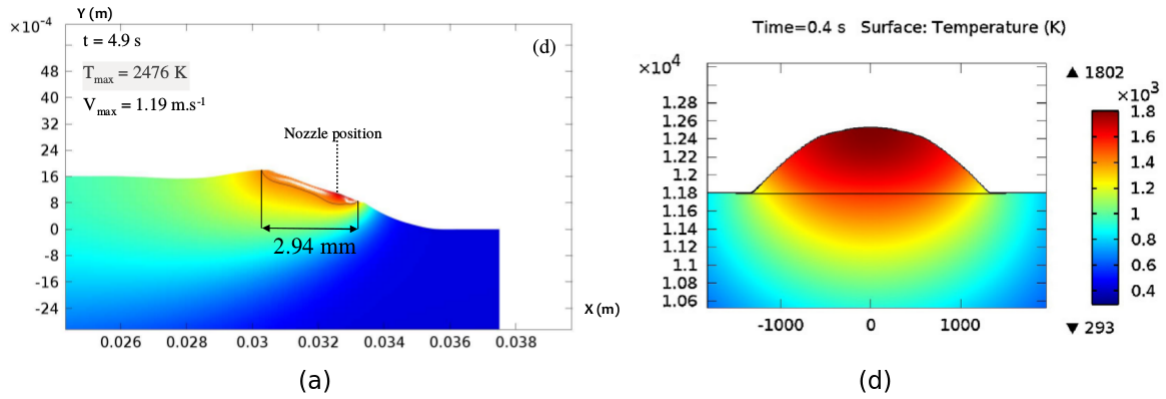


Figure 33: ALE moving mesh technique in 2D simulations presented by Morveille [218] (a) and Ya [219] (b).

To conclude, the 2D models provide supplementary results with acceptable computational time, while the assumption neglecting transverse fluid flow leads to low accuracy and predictive. Similarly, ALE moving mesh technique has also applied to 3D simulation. Gan *et al.* [176] simulated laser-assisted additive manufacturing, the mass addition is represented by the moving velocity of liquid/gas interface (see equation 32). Figure 34 shows the simulation results of DED by employing ALE moving mesh technique.

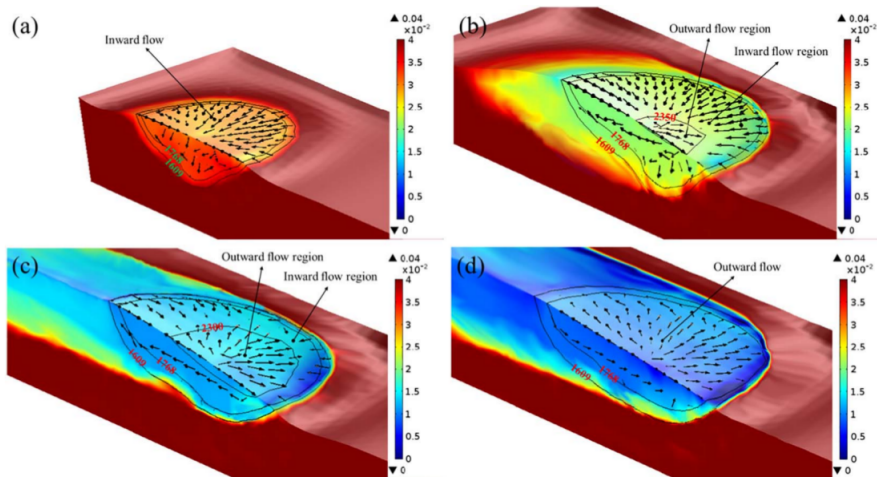


Figure 34: Application of ALE moving mesh for DED simulation in 3D, adapted from [176].

Apart from aforementioned single-material FEM method, the FVM method has also been widely used to model the DED process, and both gas and liquid/solid material will be modeled. The liquid/solid-gas interface is tracked by VOF [222] or level-set [192; 223]. The concept of VOF and Level-set method has already been introduced in section 4.2, while we discuss their applications for taking mass addition into account. The interface capturing method in VOF has initially been proposed for welding simulation [224], nowadays, this technique has been widely used to model the DED process in FVM [225]. The liquid-gas interface profile is calculated by minimizing the total energy of the surface, and the melt pool surface profile during gas metal arc welding [224], is controlled by following equations:

$$\gamma \left[ \frac{(1 + \phi_y^2) \phi_{xx} - 2\phi_x \phi_y \phi_{xy} + (1 + \phi_x^2) \phi_{yy}}{(1 + \phi_x^2 + \phi_y^2)^{3/2}} \right] = \rho g \phi + P_a + \lambda \quad (34)$$

$$\int \int (\phi_s - z_0) dx dy - \frac{\pi r_w^2 w_f}{U_w} = 0$$

where  $\phi$  is the general variable; subscript  $x$  and  $y$  stands for partial derivative to  $x$  and  $y$ ;  $\gamma$  and  $\lambda$  are the surface tension and Lagrange multiplier, respectively.  $\phi_s - z_0$  is the difference between solidified surface profile and initial  $z$  location of specimen top surface;  $r_w$ ,  $w_f$  and  $U_w$  represent the wire radius, wire feeding rate and the source traveling speed. In the context of DED, the term  $\frac{\pi r_w^2 w_f}{U_w}$  should be reformulated as  $\frac{\eta_p m}{\rho_p U_w}$  to represent the evolution of metal volume due to mass addition of powder particles.

The level-set method used to model DED is based on the same idea presented in Section 4.2, and the only modification made for equation 19 is the calculation of speed function  $v_N$ . According to the physics of the DED process, the  $v_N$  can be addition of two parts : (i) velocity solution of Navier-Stokes equation; (ii) velocity related to mass addition. The  $v_N$  can be calculated in the similar way presented in equation 32. The continuum material properties in different levels are solved in the same way presented in Section 4.2.

Figure 35 shows two examples of DED simulations. Both VOF method and LS method can give similar features in terms of simulation capacities.

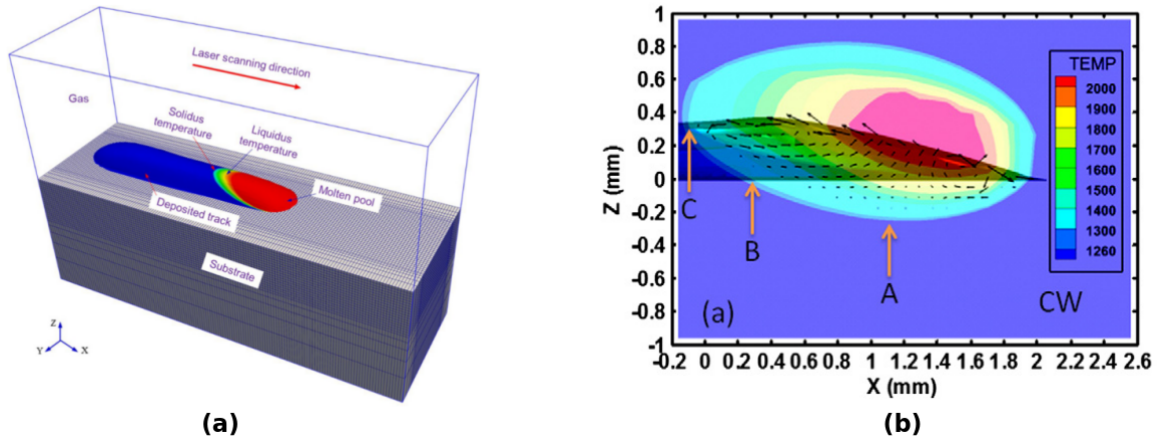


Figure 35: Applications of VOF [222] (a) and LS [223] method (b) for DED simulation.

#### 4.4.2. molten pool models with powder feeding

Aforementioned molten pool models without powder feeding provide possibility of simulating the melting profile and temperature evolution during DED process. However, the precision of prediction is limited by the assumptions made for these models. For example, the powder falling in the region of melt pool is melted immediately and they are assumed to be the same temperature as the melt pool; the momentum quantity associate with the powder addition is neglected. Actually, The study of Bayat *et al.* [226] presents that the incoming powder can affect the movement of fluid flow in melt pool, which can further change the temperature distribution and melt pool profile. For example, the melt pool becomes both narrower and colder with increasing powder speed, and the melt pool velocity magnitude decreases with the increase of the particles speed. Therefore, considering the enthalpy and momentum of powder is crucial for improving the prediction precision of numerical models in DED.

To take into account the effects (momentum, enthalpy) of incoming powder on melt pool, the FVM method with VOF [226] and FEM method with conservative level set method [227] have been applied to simulate DED process. These models will model two-phase flow problems (gas and metal). Figure 36 presents two respective simulations of molten pool models incorporated with powder feeding, and the laser attenuation are taken into account directly by applying

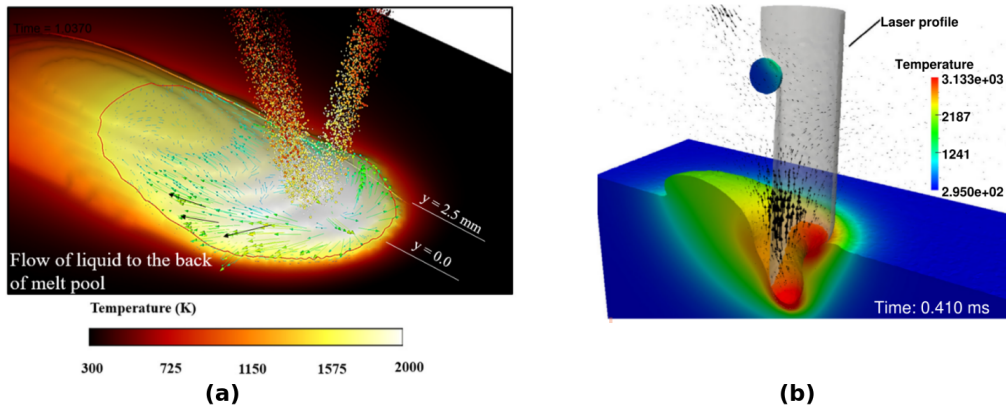


Figure 36: Molten pool models with powder feeding simulation: VOF [226] (a) and LS [227] method (b).

Lambert-Beer theorem. These models can give the most realistic simulations. However, the mesh should be fine enough (in several micrometer) to capture the geometry and movement of powder particles, and the fine mesh would lead to a considerable increasing of computational cost.

## 5. Conclusions and perspectives

In this paper, a comprehensive analysis and presentation of modeling techniques developed for the simulation of powder-based AM are reviewed. This review starts from the presentation of pure heat transfer models until the most complex multiphysics models, which will allow the reader a better understanding of the advantages and drawbacks of different numerical models. As it can be seen from figure 37, the organization of paper is from top to down : part-scale models, meso-scale models, and powder-scale models.

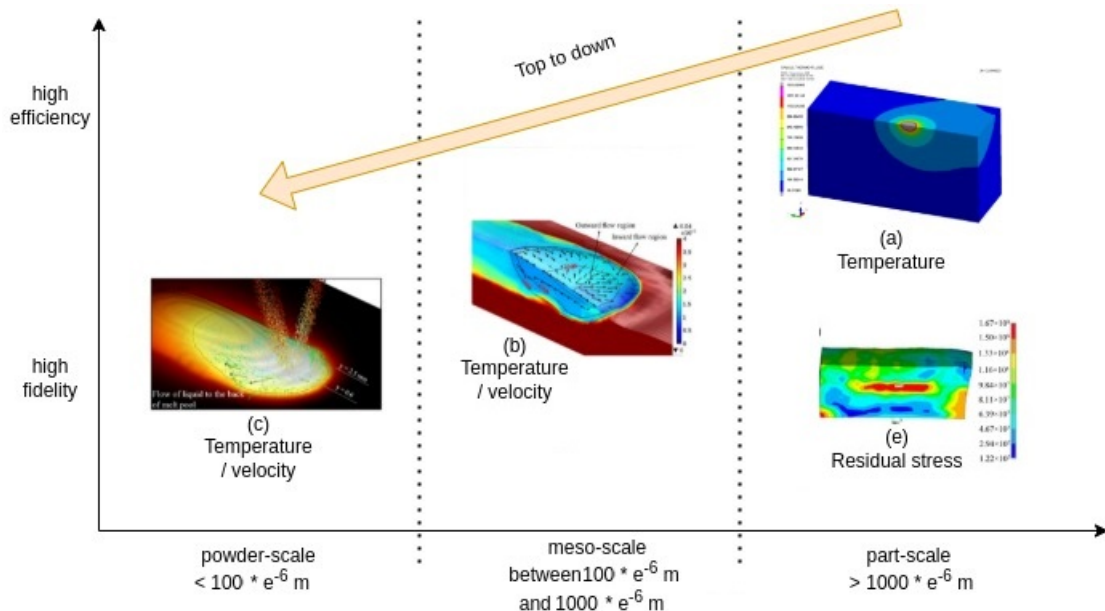


Figure 37: Overview of relationship of different modeling scales: adapted from (b) [176]; (c) [226]; (e) [12].

The part-scale models consist of solving heat transfer equation in thermal analysis and equilibrium equations in mechanical analysis. The key of such type of modelings is heat source fitting procedure, as the heat convection in

melt pool is disregarded; therefore, the heat source should be calibrated according to experimental results. These simplifications can reduce significantly the computational cost, while the precision of prediction is not guaranteed for the process parameters without experiments. Apart from computational efficiency, the part-scale models provide the possibility of computing the distortions and residual stresses of manufactured parts. Different frameworks for accelerating thermal and mechanical analysis proposed in the literature are discussed and compared together. However, the mechanical material behaviour during the manufacturing processes, especially for multi-cycles of rapid heating and cooling, still requires more investigations.

The powder-scale models considers the real geometry of powder particles and allows taking the fluid-flow in melting pool, laser-powder and gas-material interactions into account, which can significantly improve the precision of predictions. Moreover, the powder-scale models can also investigate the keyhole induced porosity as well as formation of lack of fusion related to process parameters. Since these models work on the powder scale, the computational cost of powder-scale models is still its main obstacle.

The meso-scale models can be considered as a compromise solution between the powder-scale and part-scale models. Such alternative considers the fluid-flow simulation in melt pool, while the powder layer is treated as a continuum medium with different thermal properties from the compact state. Compared to the powder-scale models, the simplification conducted by using the continuum medium allows utilization of larger size element, thus less computational cost can be expected.

The selection of a numerical model depends on predefined research objectives and computational constraints. An effective numerical model should efficiently achieve these objectives while minimizing computational resources. Consider the example of investigating the influence of powder shape: only powder-scale models can accurately account for powder shape effects. If one would like investigate the relationship between the print order and the residual deformation, the part-scale model is most suitable. This underscores the necessity of aligning the chosen numerical model with the specific goals of the investigation, ensuring that the computational cost is appropriately balanced against the insights gained.

Future developments in this field can be categorized into following directions:

1. **High-Fidelity multiphysics computational models:** The focus here is on creating comprehensive multiphysics models that capture a wide range of physical phenomena. This could include incorporating considerations like grain orientation during solidification and its mechanical properties at grain scale and addressing challenges such as fissure formation inter grain. The aim is to develop models that reflect the real-world processes as accurately as possible, enhancing the predictive capabilities and insight gained from simulations, which allows aiding designs of new materials and alloy with specific properties.
2. **High-Efficiency part-scale computational models:** Another promising direction for development is the creation of highly efficient models specifically designed for individual parts. These models aim to strike a balance between computational cost and accuracy, addressing the challenge of predicting residual stress and distortion in manufactured parts. This challenge becomes even more critical as manufactured parts can consist of hundreds of layers or even more, demanding efficient computational strategies that can handle the intricacies of layer-wise manufacturing processes.
3. **Machine learning and additive manufacturing:** The field of additive manufacturing has seen an explosive growth in databases, both experimental and numerical. Machine learning offer an exciting opportunity for exploring the data to uncover hidden relationships between input parameters and some specific properties of manufactured parts [228; 229].

## References

- [1] H.R. Kotadia, G. Gibbons, A. Das, and P.D. Howes. A review of laser powder bed fusion additive manufacturing of aluminium alloys: Microstructure and properties. *Additive Manufacturing*, 46:102155, 2021.
- [2] Stefan Pfeiffer, Kevin Florio, Dario Puccio, Marco Grasso, Bianca Maria Colosimo, Christos G. Aneziris, Konrad Wegener, and Thomas Graule. Direct laser additive manufacturing of high performance oxide ceramics: A state-of-the-art review. *Journal of the European Ceramic Society*, 2021.
- [3] Byron Blakey-Milner, Paul Gradl, Glen Snedden, Michael Brooks, Jean Pitot, Elena Lopez, Martin Leary, Filippo Berto, and Anton du Plessis. Metal additive manufacturing in aerospace: A review. *Materials & Design*, 209:110008, 2021.
- [4] Meisam Askari, David A. Hutchins, Peter J. Thomas, Lorenzo Astolfi, Richard L. Watson, Meisam Abdi, Marco Ricci, Stefano Laureti, Luzhen Nie, Steven Freear, Ricky Wildman, Christopher Tuck, Matt Clarke, Emma Woods, and Adam T. Clare. Additive manufacturing of metamaterials: A review. *Additive Manufacturing*, 36:101562, 2020.
- [5] Nesma T. Aboulkhair, Marco Simonelli, Luke Parry, Ian Ashcroft, Christopher Tuck, and Richard Hague. 3d printing of aluminium alloys: Additive manufacturing of aluminium alloys using selective laser melting. *Progress in Materials Science*, 106:100578, 2019.
- [6] Yassine Saadlaoui, Jean-Louis Milan, Jean-Marie Rossi, and Patrick Chabrand. Topology optimization and additive manufacturing: Comparison of conception methods using industrial codes. *Journal of Manufacturing Systems*, 43:178–186, 2017.
- [7] Yoram Mass and Oded Amir. Topology optimization for additive manufacturing: Accounting for overhang limitations using a virtual skeleton. *Additive Manufacturing*, 18:58–73, 2017.
- [8] Xu Guo, Jianhua Zhou, Weisheng Zhang, Zongliang Du, Chang Liu, and Ying Liu. Self-supporting structure design in additive manufacturing through explicit topology optimization. *Computer Methods in Applied Mechanics and Engineering*, 323:27–63, 2017.
- [9] S. Pratheesh Kumar, S. Elangovan, R. Mohanraj, and J.R. Ramakrishna. A review on properties of inconel 625 and inconel 718 fabricated using direct energy deposition. *Materials Today: Proceedings*, 2021.
- [10] Alfredo Suárez, Eider Aldalur, Fernando Veiga, Teresa Artaza, Iván Taberero, and Aitzol Lamikiz. Wire arc additive manufacturing of an aeronautic fitting with different metal alloys: From the design to the part. *Journal of Manufacturing Processes*, 64:188–197, 2021.
- [11] Mahmoud Moradi, Arman Hasani, Zeynab Pourmand, and Jonathan Lawrence. Direct laser metal deposition additive manufacturing of inconel 718 superalloy: Statistical modelling and optimization by design of experiments. *Optics & Laser Technology*, 144:107380, 2021.
- [12] Ze-Chen Fang, Zhi-Lin Wu, Chen-Guang Huang, and Chen-Wu Wu. Review on residual stress in selective laser melting additive manufacturing of alloy parts. *Optics & Laser Technology*, 129:106283, 2020.
- [13] Wan neng Zhang, Lin zhi Wang, Zhong xue Feng, and Yu ming Chen. Research progress on selective laser melting (slm) of magnesium alloys: A review. *Optik*, 207:163842, 2020.
- [14] Yang Li, Xiaoyu Liang, Yefeng Yu, Hongxin Li, Wenbin Kan, and Feng Lin. Microstructures and mechanical properties evolution of in939 alloy during electron beam selective melting process. *Journal of Alloys and Compounds*, 883:160934, 2021.
- [15] Tack Lee, Kenta Aoyagi, Huakang Bian, Kenta Yamanaka, Shigeo Sato, and Akihiko Chiba. The microstructure and mechanical properties of selective electron beam melting manufactured 9–12cr ferritic/martensitic steel using n- and ar-atomized powder. *Additive Manufacturing*, 45:102075, 2021.
- [16] Ronan McCann, Muhannad A. Obeidi, Cian Hughes, Éanna McCarthy, Darragh S. Egan, Rajani K. Vijayaraghavan, Ajey M. Joshi, Victor Acinas Garzon, Denis P. Dowling, Patrick J. McNally, and Dermot Brabazon. In-situ sensing, process monitoring and machine control in laser powder bed fusion: A review. *Additive Manufacturing*, 45:102058, 2021.
- [17] Galina Kasperovich, Jan Haubrich, Joachim Gussone, and Guillermo Requena. Correlation between porosity and processing parameters in tial6v4 produced by selective laser melting. *Materials & Design*, 105:160–170, 2016.
- [18] Christian Weingarten, Damien Buchbinder, Norbert Pirch, Wilhelm Meiners, Konrad Wissenbach, and Reinhart Poprawe. Formation and reduction of hydrogen porosity during selective laser melting of als10mg. *Journal of Materials Processing Technology*, 221:112–120, 2015.
- [19] Naor Elad Uzan, Shlomo Ramati, Roni Shneck, Nachum Frage, and Ori Yeheskel. On the effect of shot-peening on fatigue resistance of als10mg specimens fabricated by additive manufacturing using selective laser melting (am-slm). *Additive Manufacturing*, 21:458–464, 2018.
- [20] Yanjin Lu, Songquan Wu, Yiliang Gan, Tingting Huang, Chuanguang Yang, Lin Junjie, and Jinxin Lin. Study on the microstructure, mechanical property and residual stress of slm inconel-718 alloy manufactured by differing island scanning strategy. *Optics & Laser Technology*, 75:197–206, 2015.
- [21] Yang Liu, Yongqiang Yang, and Di Wang. A study on the residual stress during selective laser melting (slm) of metallic powder. *The International Journal of Advanced Manufacturing Technology*, 87(1):647–656, 2016.
- [22] Tatiana Mishurova, Sandra Cabeza, Tobias Thiede, Naresh Nadammal, Arne Kromm, Manuela Klaus, Christoph Genzel, Christoph Haberland, and Giovanni Bruno. The influence of the support structure on residual stress and distortion in slm inconel 718 parts. *Metallurgical and materials transactions A*, 49(7):3038–3046, 2018.
- [23] Wolfgang Tillmann, Nelson Filipe Lopes Dias, Dominic Stangier, Leif Hagen, Mirko Schaper, Florian Hengsbach, and Kay-Peter Hoyer. Tribo-mechanical properties and adhesion behavior of dlc coatings sputtered onto 36nicrmo16 produced by selective laser melting. *Surface and Coatings Technology*, 394:125748, 2020.
- [24] Zhibo Luo and Yaoyao Zhao. A survey of finite element analysis of temperature and thermal stress fields in powder bed fusion additive manufacturing. *Additive Manufacturing*, 21:318–332, 2018.
- [25] Matthias Markl and Carolin Körner. Multiscale modeling of powder bed-based additive manufacturing. *Annual Review of Materials Research*, 46:93–123, 08 2016.
- [26] Christoph Meier, Ryan Penny, Yu Zou, Jonathan Gibbs, and A Hart. Thermophysical phenomena in metal additive manufacturing by selective laser melting: Fundamentals, modeling, simulation and experimentation. *Annual Review of Heat Transfer*, 20, 01 2018.
- [27] Wayne King, A. Anderson, Robert Ferencz, N. Hodge, C. Kamath, and Saad Khairallah. Overview of modelling and simulation of metal powder bed fusion process at lawrence livermore national laboratory. *Materials Science and Technology*, 31:957–968, 05 2015.
- [28] Jamison L. Bartlett and Xiaodong Li. An overview of residual stresses in metal powder bed fusion. *Additive Manufacturing*, 27:131–149, 2019.



- [29] Leonardo Bertini, Francesco Bucchi, Francesco Frendo, Mattia Moda, and Bernardo Monelli. Residual stress prediction in selective laser melting: A critical review of simulation strategies. *The International Journal of Advanced Manufacturing Technology*, 105, 11 2019.
- [30] Peter S Cook and Anthony B Murphy. Simulation of melt pool behaviour during additive manufacturing: Underlying physics and progress. *Additive Manufacturing*, 31:100909, 2020.
- [31] H.L. Wei, T. Mukherjee, W. Zhang, J.S. Zuback, G.L. Knapp, A. De, and T. DebRoy. Mechanistic models for additive manufacturing of metallic components. *Progress in Materials Science*, 116:100703, 2021.
- [32] Mohamad Bayat, Wen Dong, Jesper Thorborg, Albert C. To, and Jesper H. Hattel. A review of multi-scale and multi-physics simulations of metal additive manufacturing processes with focus on modeling strategies. *Additive Manufacturing*, 47:102278, 2021.
- [33] Andrew J. Pinkerton. Advances in the modeling of laser direct metal deposition. *Journal of Laser Applications*, 27(S1):S15001, 2015.
- [34] Xiaoyi Guan and Yaoyao Zhao. Modeling of the laser powder-based directed energy deposition process for additive manufacturing: a review. *The International Journal of Advanced Manufacturing Technology*, 107, 03 2020.
- [35] C. C. Ng, M. M. Savalani, H. C. Man, and I. Gibson. Layer manufacturing of magnesium and its alloy structures for future applications. *Virtual and Physical Prototyping*, 5(1):13–19, 2010.
- [36] E.O. Olakanmi, R.F. Cochrane, and K.W. Dalgarno. A review on selective laser sintering/melting (sls/slm) of aluminium alloy powders: Processing, microstructure, and properties. *Progress in Materials Science*, 74:401–477, 2015.
- [37] Nesma T. Aboulkhair, Nicola M. Everitt, Ian Ashcroft, and Chris Tuck. Reducing porosity in alsi10mg parts processed by selective laser melting. *Additive Manufacturing*, 1-4:77–86, 2014.
- [38] J.X. Fang, S.Y. Dong, S.B. Li, Y.J. Wang, B.S. Xu, J. Li, B. Liu, and Y.L. Jiang. Direct laser deposition as repair technology for a low transformation temperature alloy: Microstructure, residual stress, and properties. *Materials Science and Engineering: A*, 748:119–127, 2019.
- [39] Sulochana Shrestha, Joseph El Rassi, Manigandan Kannan, Gregory Morscher, Andrew L. Gyekenyesi, and Onome E. Scott-Emuakpor. Fracture toughness and fatigue crack growth rate properties of am repaired ti–6al–4v by direct energy deposition. *Materials Science and Engineering: A*, 823:141701, 2021.
- [40] Z.D. Wang, G.F. Sun, M.Z. Chen, Y. Lu, S.B. Zhang, H.F. Lan, K.D. Bi, and Z.H. Ni. Investigation of the underwater laser directed energy deposition technique for the on-site repair of hsla-100 steel with excellent performance. *Additive Manufacturing*, 39:101884, 2021.
- [41] C. Scheitler, F. Hugger, K. Hofmann, O. Hentschel, T. Baetzler, S. Roth, and M. Schmidt. Experimental investigation of direct diamond laser cladding in combination with high speed camera based process monitoring. *Journal of Laser Applications*, 28(2):022304, 2016.
- [42] Xufei Lu, Xin Lin, Michele Chiumenti, Miguel Cervera, JunJie Li, Liang Ma, Lei Wei, Yunlong Hu, and Weidong Huang. Finite element analysis and experimental validation of the thermomechanical behavior in laser solid forming of ti-6al-4v. *Additive Manufacturing*, 21:30–40, 2018.
- [43] Peter S Cook and Anthony B Murphy. Simulation of melt pool behaviour during additive manufacturing: Underlying physics and progress. *Additive Manufacturing*, 31:100909, 2020.
- [44] S Cadiou, M Courtois, M Carin, W Berckmans, and P Le Masson. Heat transfer, fluid flow and electromagnetic model of droplets generation and melt pool behaviour for wire arc additive manufacturing. *International Journal of Heat and Mass Transfer*, 148:119102, 2020.
- [45] Cassiopée Galy, Emilie Le Guen, Eric Lacoste, and Corinne Arvieu. Main defects observed in aluminum alloy parts produced by slm: from causes to consequences. *Additive manufacturing*, 22:165–175, 2018.
- [46] E Feulvarch, V Robin, and J M Bergheau. Thermometallurgical and mechanical modelling of welding – application to multipass dissimilar metal girth welds. *Science and Technology of Welding and Joining*, 16(3):221–231, 2011.
- [47] H.M. Aarbogh, M. Hamide, H.G. Fjær, A. Mo, and M. Bellet. Experimental validation of finite element codes for welding deformations. *Journal of Materials Processing Technology*, 210(13):1681–1689, 2010.
- [48] Dieter Radaj. *Heat effects of welding: temperature field, residual stress, distortion*. Springer Science & Business Media, 2012.
- [49] X.K. Zhu and Y.J. Chao. Effects of temperature-dependent material properties on welding simulation. *Computers & Structures*, 80(11):967–976, 2002.
- [50] Yabo Jia, Jean-Michel Bergheau, Jean-Baptiste Leblond, Jean-Christophe Roux, Raihane Bouchaoui, Sebastien Gallée, and Alexandre Brosse. A new nodal-integration-based finite element method for the numerical simulation of welding processes. *Metals*, 10(10), 2020.
- [51] P. Duranton, J. Devaux, V. Robin, P. Gilles, and J.M. Bergheau. 3d modelling of multipass welding of a 316l stainless steel pipe. *Journal of Materials Processing Technology*, 153-154:457–463, 2004. Proceedings of the International Conference in Advances in Materials and Processing Technologies.
- [52] Andrés Anca, Víctor D. Fachinotti, Gustavo Escobar-Palafox, and Alberto Cardona. Computational modelling of shaped metal deposition. *International Journal for Numerical Methods in Engineering*, 85(1):84–106, 2011.
- [53] Michele Chiumenti, Miguel Cervera, Alessandro Salmi, Carlos Agelet de Saracibar, Narges Dialami, and Kazumi Matsui. Finite element modeling of multi-pass welding and shaped metal deposition processes. *Computer Methods in Applied Mechanics and Engineering*, 199(37):2343–2359, 2010.
- [54] Andreas Lundbäck and Lars-Erik Lindgren. Modelling of metal deposition. *Finite Elements in Analysis and Design*, 47(10):1169–1177, 2011.
- [55] Loucas Papadakis, Andreas Loizou, Jeroen Risse, Sebastian Bremen, and Johannes Schrage. A computational reduction model for appraising structural effects in selective laser melting manufacturing. *Virtual and Physical Prototyping*, 9(1):17–25, 2014.
- [56] O. Desmaison, P.-A. Pires, G. Levesque, A. Peralta, S. Sundarraj, A. Makinde, V. Jagdale, and M. Megahed. Influence of computational grid and deposit volume on residual stress and distortion prediction accuracy for additive manufacturing modeling. In Paul Mason, Charles R. Fisher, Ryan Glamm, Michele V. Manuel, Georg J. Schmitz, Amarendra K. Singh, and Alejandro Strachan, editors, *Proceedings of the 4th World Congress on Integrated Computational Materials Engineering (ICME 2017)*, pages 365–374, Cham, 2017. Springer International Publishing.
- [57] Panagiotis Michaleris. Modeling metal deposition in heat transfer analyses of additive manufacturing processes. *Finite Elements in Analysis and Design*, 86:51–60, 2014.
- [58] L. Wang, S. Felicelli, Y. Gooroochurn, P. Wang, and M. F. Horstemeyer. Numerical simulation of the temperature distribution and solid-phase evolution in the lenstm process. 2006.
- [59] Lars-Erik Lindgren, Henrik Runnemalm, and Mats O. Näsström. Simulation of multipass welding of a thick plate. *International Journal for*

- Numerical Methods in Engineering*, 44(9):1301–1316, 1999.
- [60] R. Jendrzewski, G. Śliwiński, M. Krawczuk, and W. Ostachowicz. Temperature and stress fields induced during laser cladding. *Computers & Structures*, 82(7):653–658, 2004.
- [61] Riqing Ye, John E. Smugeresky, Baolong Zheng, Yizhang Zhou, and Enrique J. Lavernia. Numerical modeling of the thermal behavior during the lens® process. *Materials Science and Engineering: A*, 428(1):47–53, 2006.
- [62] P Peyre, P Aubry, R Fabbro, R Neveu, and A Longuet. Analytical and numerical modelling of the direct metal deposition laser process. *Journal of Physics D: Applied Physics*, 41(2):025403, jan 2008.
- [63] F. Fanicchia and D.A. Axinte. Transient three-dimensional geometrical/thermal modelling of thermal spray: Normal-impinging jet and single straight deposits. *International Journal of Heat and Mass Transfer*, 122:1327–1342, 2018.
- [64] Qingcheng Yang, Pu Zhang, Lin Cheng, Zheng Min, Minking Chyu, and Albert C. To. Finite element modeling and validation of thermomechanical behavior of ti-6al-4v in directed energy deposition additive manufacturing. *Additive Manufacturing*, 12:169–177, 2016. Special Issue on Modeling & Simulation for Additive Manufacturing.
- [65] I. Taberero, A. Lamikiz, E. Ukar, S. Martínez, and A. Celaya. Modeling of the geometry built-up by coaxial laser material deposition process. *The International Journal of Advanced Manufacturing Technology*, 70:843–851, 2014.
- [66] E. Ukar, A. Lamikiz, L. N. López de Lacalle, S. Martínez, F. Liébana, and Taberero. Thermal model with phase change for process parameter determination in laser surface processing. *Physics Procedia*, 5:395–403, January 2010.
- [67] I. Taberero, A. Lamikiz, E. Ukar, L.N. López de Lacalle, C. Angulo, and G. Urbikain. Numerical simulation and experimental validation of powder flux distribution in coaxial laser cladding. *Journal of Materials Processing Technology*, 210(15):2125–2134, 2010.
- [68] Eric Feulvarch, François Josse, Jean-Christophe Roux, and Alexey Sova. An efficient reduced-physics-coupling fem formulation for simulating a molten metal deposition geometry. *European Journal of Mechanics - A/Solids*, 89:104290, 2021.
- [69] Jean-Baptiste Leblond, Hussein Amin El Sayed, and Jean-Michel Bergheau. On the incorporation of surface tension in finite-element calculations. *Comptes Rendus Mécanique*, 341(11):770–775, 2013.
- [70] C. Bonacina, G. Comini, A. Fasano, and M. Primicerio. Numerical solution of phase-change problems. *International Journal of Heat and Mass Transfer*, 16(10):1825–1832, 1973.
- [71] Ahmed Hussein, Liang Hao, Chunze Yan, and Richard Everson. Finite element simulation of the temperature and stress fields in single layers built without-support in selective laser melting. *Materials & Design (1980-2015)*, 52:638–647, 2013.
- [72] I.A. Roberts, C.J. Wang, R. Esterlein, M. Stanford, and D.J. Mynors. A three-dimensional finite element analysis of the temperature field during laser melting of metal powders in additive layer manufacturing. *International Journal of Machine Tools and Manufacture*, 49(12):916–923, 2009.
- [73] C. H. Fu and Y. B. Guo. Three-Dimensional Temperature Gradient Mechanism in Selective Laser Melting of Ti-6Al-4V. *Journal of Manufacturing Science and Engineering*, 136(6), 10 2014. 061004.
- [74] Carolin Körner, Elham Attar, and Peter Heintl. Mesoscopic simulation of selective beam melting processes. *Journal of Materials Processing Technology*, 211(6):978–987, 2011.
- [75] Yabo Jia, Yassine Saadlaoui, and Jean-Michel Bergheau. A temperature-dependent heat source for simulating deep penetration in selective laser melting process. *Applied Sciences*, 11(23):11406, Dec 2021.
- [76] Yabo Jia, Yassine Saadlaoui, Hédi Hamdi, Julien Sijobert, Jean-Christophe Roux, and Jean-Michel Bergheau. An experimental and numerical case study of thermal and mechanical consequences induced by laser welding process. *Case Studies in Thermal Engineering*, 35:102078, 2022.
- [77] Paolo Ferro, Andrea Zambon, and Franco Bonollo. Investigation of electron-beam welding in wrought inconel 706—experimental and numerical analysis. *Materials Science and Engineering: A*, 392(1):94–105, 2005.
- [78] Jazeel Rahman Chukkan, M. Vasudevan, S. Muthukumar, R. Ravi Kumar, and N. Chandrasekhar. Simulation of laser butt welding of aisi 316l stainless steel sheet using various heat sources and experimental validation. *Journal of Materials Processing Technology*, 219:48–59, 2015.
- [79] M. Dal and R. Fabbro. [invited] an overview of the state of art in laser welding simulation. *Optics & Laser Technology*, 78:2–14, 2016. The year of light: optical fiber sensors and laser material processing.
- [80] Shiwen Liu, Haihong Zhu, Gangyong Peng, Jie Yin, and Xiaoyan Zeng. Microstructure prediction of selective laser melting als10mg using finite element analysis. *Materials & Design*, 142:319–328, 2018.
- [81] J. Goldak, A. P. Chakravarti, and M. Bibby. A new finite element model for welding heat sources. *Metallurgical Transactions B*, 15:299–305, 1984.
- [82] Yabo Jia, Jean-Michel Bergheau, Jean-Baptiste Leblond, Jean-Christophe Roux, Raihane Bouchaoui, Sebastien Gallée, and Alexandre Brosse. A new nodal-integration-based finite element method for the numerical simulation of welding processes. *Metals*, 10(10):1386, Oct 2020.
- [83] Bo Cheng and Kevin Chou. Geometric consideration of support structures in part overhang fabrications by electron beam additive manufacturing. *Computer-Aided Design*, 69:102–111, 2015.
- [84] Wentao Yan, Jacob Smith, Wenjun Ge, Feng Lin, and Wing Kam Liu. Multiscale modeling of electron beam and substrate interaction: A new heat source model. *Comput. Mech.*, 56(2):265–276, August 2015.
- [85] Yi Luo, Jinhe Liu, and Hong Ye. An analytical model and tomographic calculation of vacuum electron beam welding heat source. *Vacuum*, 84(6):857–863, 2010.
- [86] Yassine Saadlaoui, Julien Sijobert, Maria Doubenskaia, Philippe Bertrand, Eric Feulvarch, and Jean-Michel Bergheau. Experimental study of thermomechanical processes: Laser welding and melting of a powder bed. *Crystals*, 10(4), 2020.
- [87] T. DebRoy, H.L. Wei, J.S. Zuback, T. Mukherjee, J.W. Elmer, J.O. Milewski, A.M. Beese, A. Wilson-Heid, A. De, and W. Zhang. Additive manufacturing of metallic components – process, structure and properties. *Progress in Materials Science*, 92:112–224, 2018.
- [88] T. Debroy and S.A. David. Physical processes in fusion welding. *Reviews of Modern Physics*, 67(1):85–112, 1995. cited By 381.
- [89] T. Mukherjee, H.L. Wei, A. De, and T. DebRoy. Heat and fluid flow in additive manufacturing – part ii: Powder bed fusion of stainless steel, and titanium, nickel and aluminum base alloys. *Computational Materials Science*, 150:369–380, 2018.
- [90] Jon Iñaki Arrizubieta, Aitzol Lamikiz, Fritz Klocke, Silvia Martínez, Kristian Arntz, and Eneko Ukar. Evaluation of the relevance of melt

- pool dynamics in laser material deposition process modeling. *International Journal of Heat and Mass Transfer*, 115:80–91, 2017.
- [91] Guillaume Tirand, Corinne Arvieu, Eric Lacoste, and Jean-Michel Quenisset. Control of aluminium laser welding conditions with the help of numerical modelling. *Journal of Materials Processing Technology*, 213(3):337–348, 2013.
- [92] A M Kamara, W Wang, S Marimuthu, and L Li. Modelling of the melt pool geometry in the laser deposition of nickel alloys using the anisotropic enhanced thermal conductivity approach. *Proceedings of the Institution of Mechanical Engineers, Part B: Journal of Engineering Manufacture*, 225(1):87–99, 2011.
- [93] Emilie Le Guen, Rémy Fabbro, Frédéric Coste, Muriel Carin, and Philippe Le Masson. Physical study of hybrid nd:yag laser-mag welding process. *International Congress on Applications of Lasers & Electro-Optics*, 2009(1):1532–1537, 2009.
- [94] Andrés Anca, Alberto Cardona, José Risso, and Víctor D. Fachinotti. Finite element modeling of welding processes. *Applied Mathematical Modelling*, 35(2):688–707, 2011.
- [95] Guangming Fu, Jijun Gu, Marcelo Igor Lourenco, Menglan Duan, and Segen F. Estefen. Parameter determination of double-ellipsoidal heat source model and its application in the multi-pass welding process. *Ships and Offshore Structures*, 10(2):204–217, 2015.
- [96] A. Belitzki, C. Marder, A. Huisel, and M. Zaeh. Automated heat source calibration for the numerical simulation of laser beam welded components. *Production Engineering*, 10, 02 2016.
- [97] T.R. Walker and C.J. Bennett. An automated inverse method to calibrate thermal finite element models for numerical welding applications. *Journal of Manufacturing Processes*, 47:263–283, 2019.
- [98] Yali Li and Dongdong Gu. Thermal behavior during selective laser melting of commercially pure titanium powder: Numerical simulation and experimental study. *Additive Manufacturing*, 1-4:99–109, 2014. Inaugural Issue.
- [99] Patcharapit Promopattum, Recep Onler, and Shi-Chune Yao. Numerical and experimental investigations of micro and macro characteristics of direct metal laser sintered ti-6al-4v products. *Journal of Materials Processing Technology*, 240:262–273, 2017.
- [100] Frederic E. Bock, Jan Herrnring, Martin Froend, Josephin Enz, Nikolai Kashaev, and Benjamin Klusemann. Experimental and numerical thermo-mechanical analysis of wire-based laser metal deposition of al-mg alloys. *Journal of Manufacturing Processes*, 64:982–995, 2021.
- [101] S. Kolossov, E. Boillat, R. Glardon, P. Fischer, and M. Locher. 3d fe simulation for temperature evolution in the selective laser sintering process. *International Journal of Machine Tools and Manufacture*, 44(2):117–123, 2004.
- [102] L. Dong, A. Makradi, S. Ahzi, and Y. Remond. Three-dimensional transient finite element analysis of the selective laser sintering process. *Journal of Materials Processing Technology*, 209(2):700–706, 2009.
- [103] Loong-Ee Loh, Chee-Kai Chua, Wai-Yee Yeong, Jie Song, Mahta Mapar, Swee-Leong Sing, Zhong-Hong Liu, and Dan-Qing Zhang. Numerical investigation and an effective modelling on the selective laser melting (slm) process with aluminium alloy 6061. *International Journal of Heat and Mass Transfer*, 80:288–300, 2015.
- [104] Erik R. Denlinger, Vijay Jagdale, G.V. Srinivasan, Tahany El-Wardany, and Pan Michaleris. Thermal modeling of inconel 718 processed with powder bed fusion and experimental validation using in situ measurements. *Additive Manufacturing*, 11:7–15, 2016.
- [105] G.R. Hadley. Thermal conductivity of packed metal powders. *International Journal of Heat and Mass Transfer*, 29(6):909–920, 1986.
- [106] Samuel Sumin Sih and Joel W Barlow. Measurement and prediction of the thermal conductivity of powders at high temperatures. *Solid Freeform Fabrication*, 321, 1994.
- [107] Sakae Yagi and Daizo Kunii. Studies on effective thermal conductivities in packed beds. *AIChE Journal*, 3(3):373–381, 1957.
- [108] Kurian Antony, N. Arivazhagan, and K. Senthilkumaran. Numerical and experimental investigations on laser melting of stainless steel 316l metal powders. *Journal of Manufacturing Processes*, 16(3):345–355, 2014.
- [109] Patri K Venuvinod and Weiyin Ma. *Rapid prototyping: laser-based and other technologies*. Springer Science & Business Media, 2013.
- [110] G. Bugeđa, M. Cervera, and G. Lombera. Numerical prediction of temperature and density distributions in selective laser sintering processes. *Rapid Prototyping Journal*, 5(1):21–26, 1999. cited By 138.
- [111] Jie Yin, Haihong Zhu, Linda Ke, Wenjuan Lei, Cheng Dai, and Duluo Zuo. Simulation of temperature distribution in single metallic powder layer for laser micro-sintering. *Computational Materials Science*, 53(1):333–339, 2012.
- [112] Yabo Jia, Yassine Saadlaoui, and Jean-Michel Bergheau. A temperature-dependent heat source for simulating deep penetration in selective laser melting process. *Applied Sciences*, 11(23), 2021.
- [113] Software SYSWELD version 21. *Reference Analysis Manual*. Released: 2020; ESI-Group: Lyon, France, 2020.
- [114] Yabo Jia, Yassine Saadlaoui, Jean-Christophe Roux, and Jean-Michel Bergheau. Steady-state thermal model based on new dedicated boundary conditions – application in the simulation of laser powder bed fusion process. *Applied Mathematical Modelling*, 112:749–766, 2022.
- [115] Faiyaz Ahsan, Jafar Razmi, and Leila Ladani. Experimental measurement of thermal diffusivity, conductivity and specific heat capacity of metallic powders at room and high temperatures. *Powder Technology*, 374:648–657, 2020.
- [116] J.B. Leblond and J. Devaux. A new kinetic model for anisothermal metallurgical transformations in steels including effect of austenite grain size. *Acta Metallurgica*, 32(1):137–146, 1984.
- [117] D. P. Koistinen and R. E. Marburger. A general equation prescribing the extent of the austenite-martensite transformation in pure iron-carbon alloys and plain carbon steels. *Acta Metallurgica*, 7:59–60, 1959.
- [118] L.A. Parry, I.A. Ashcroft, and R.D. Wildman. Geometrical effects on residual stress in selective laser melting. *Additive Manufacturing*, 25:166–175, 2019.
- [119] L. Parry, I.A. Ashcroft, and R.D. Wildman. Understanding the effect of laser scan strategy on residual stress in selective laser melting through thermo-mechanical simulation. *Additive Manufacturing*, 12:1–15, 2016.
- [120] Wei Chen, Lianyong Xu, Yongdian Han, Lei Zhao, and Hongyang Jing. Control of residual stress in metal additive manufacturing by low-temperature solid-state phase transformation: An experimental and numerical study. *Additive Manufacturing*, 42:102016, 2021.
- [121] R.K. Ganeriwala, M. Strantza, W.E. King, B. Clausen, T.Q. Phan, L.E. Levine, D.W. Brown, and N.E. Hodge. Evaluation of a thermo-mechanical model for prediction of residual stress during laser powder bed fusion of ti-6al-4v. *Additive Manufacturing*, 27:489–502, 2019.
- [122] C. C. Murgau. Microstructure model for ti-6al-4v used in simulation of additive manufacturing. In *Ph.D.*, 2016.
- [123] N. Kotkunde, A.D. Deole, A.K. Gupta, and S.K. Singh. Comparative study of constitutive modeling for ti-6al-4v alloy at low strain rates and elevated temperatures. *Materials and Design*, 55:999–1005, 2014. cited By 110.

- [124] Patcharapit Promopattum and Anthony D. Rollett. Physics-based and phenomenological plasticity models for thermomechanical simulation in laser powder bed fusion additive manufacturing: A comprehensive numerical comparison. *Materials & Design*, 204:109658, 2021.
- [125] Xufei Lu, Michele Chiumenti, Miguel Cervera, Junjie Li, Xin Lin, Liang Ma, Guohao Zhang, and Enquan Liang. Substrate design to minimize residual stresses in directed energy deposition am processes. *Materials & Design*, 202, 02 2021.
- [126] Huayan Pu, Guan Liang, Hakim Naceur, Jinglei Zhao, Jin Yi, Jun Luo, Daniel Coutellier, Li Wang, and Ruqing Bai. Thermo-mechanical analysis of ti-6al-4v taylor bar using advanced joint path strategies based on additive manufacturing. *CIRP Journal of Manufacturing Science and Technology*, 40:167–179, 2023.
- [127] Yabo Jia, Jean-Baptiste Leblond, and Jean-Michel Bergheau. Exact satisfaction of boundary and interface conditions in nodal-integration-based finite element methods. *Comptes Rendus. Mécanique*, 350:57–83, 2022.
- [128] J Goldak, J Zhou, V Breiguine, and F Montoya. Thermal stress analysis of welds: from melting point to room temperature. *Transactions of JWRI*, 25(2):185–189, 1996.
- [129] Zhipeng Pan, Donald S Shih, Hamid Garmestani, Anthony D Rollett, and Steven Y Liang. Mts model based force prediction for machining of ti-6al-4v. *Journal of Advanced Mechanical Design, Systems, and Manufacturing*, 11(3):JAMDSM0033–JAMDSM0033, 2017.
- [130] Gbenga Asala, Joel Andersson, and Olanrewaj A Ojo. Analysis and constitutive modelling of high strain rate deformation behaviour of wire-arc additive-manufactured ati 718plus superalloy. *The International Journal of Advanced Manufacturing Technology*, 103(1-4):1419–1431, 2019.
- [131] Yanhua Zhao, Jie Sun, Jianfeng Li, Yuqin Yan, and Ping Wang. A comparative study on johnson-cook and modified johnson-cook constitutive material model to predict the dynamic behavior laser additive manufacturing fecr alloy. *Journal of Alloys and Compounds*, 723:179–187, 2017.
- [132] Xinyu Yang, Richard A. Barrett, Noel M. Harrison, and Sean B. Leen. A physically-based structure-property model for additively manufactured ti-6al-4v. *Materials & Design*, 205:109709, 2021.
- [133] Bo Cheng, Subin Shrestha, and Kevin Chou. Stress and deformation evaluations of scanning strategy effect in selective laser melting. *Additive Manufacturing*, 12:240–251, 2016. Special Issue on Modeling & Simulation for Additive Manufacturing.
- [134] K. Zeng, D. Pal, H.J. Gong, N. Patil, and B. Stucker. Comparison of 3dsim thermal modelling of selective laser melting using new dynamic meshing method to ansys. *Materials Science and Technology (United Kingdom)*, 31(8):945–956, 2015. cited By 69.
- [135] Erik R. Denlinger, Michael Gouge, Jeff Irwin, and Pan Michaleris. Thermomechanical model development and in situ experimental validation of the laser powder-bed fusion process. *Additive Manufacturing*, 16:73–80, 2017.
- [136] Joan Baiges, Michele Chiumenti, Carlos A. Moreira, Miguel Cervera, and Ramon Codina. An adaptive finite element strategy for the numerical simulation of additive manufacturing processes. *Additive Manufacturing*, 37:101650, 2021.
- [137] Mohamad Bayat, Christopher Klingaa, Sankhya Mohanty, David De Baere, J. Thorborg, Niels Tiedje, and J.H. Hattel. Part-scale thermo-mechanical modelling of distortions in laser powder bed fusion – analysis of the sequential flash heating method with experimental validation. *Additive Manufacturing*, 36:101508, 08 2020.
- [138] Michele Chiumenti, Eric Neiva, Emilio Salsi, Miguel Cervera, Santiago Badia, Joan Moya, Zhuoer Chen, Caroline Lee, and Christopher Davies. Numerical modelling and experimental validation in selective laser melting. *Additive Manufacturing*, 18:171–185, 2017.
- [139] Ming Liu, Louis N.S. Chiu, Chaitanya Vundru, Yang Liu, Aijun Huang, Chris Davies, Xinhua Wu, and Wenyi Yan. A characteristic time-based heat input model for simulating selective laser melting. *Additive Manufacturing*, 44:102026, 2021.
- [140] C. Li, J.F. Liu, X.Y. Fang, and Y.B. Guo. Efficient predictive model of part distortion and residual stress in selective laser melting. *Additive Manufacturing*, 17:157–168, 2017.
- [141] Yang Cao, Xin Lin, Nan Kang, Liang Ma, Lei Wei, Min Zheng, Jun Yu, Dongjian Peng, and Weidong Huang. A novel high-efficient finite element analysis method of powder bed fusion additive manufacturing. *Additive Manufacturing*, 46:102187, 2021.
- [142] Matteo Bugatti and Quirico Semeraro. Limitations of the inherent strain method in simulating powder bed fusion processes. *Additive Manufacturing*, 23:329–346, 2018.
- [143] Xuan Liang, Lin Cheng, Qian Chen, Qingcheng Yang, and Albert C. To. A modified method for estimating inherent strains from detailed process simulation for fast residual distortion prediction of single-walled structures fabricated by directed energy deposition. *Additive Manufacturing*, 23:471–486, 2018.
- [144] Michael R Hill and Drew V Nelson. The inherent strain method for residual stress determination and its application to a long welded joint. *ASME-PUBLICATIONS-PVP*, 318:343–352, 1995.
- [145] Nils Keller and Vasily Ploshikhin. New method for fast predictions of residual stress and distortion of am parts. In *Solid freeform fabrication symposium*, volume 25, 2014.
- [146] C. Li, C.H. Fu, Y.B. Guo, and F.Z. Fang. A multiscale modeling approach for fast prediction of part distortion in selective laser melting. *Journal of Materials Processing Technology*, 229:703–712, 2016.
- [147] T. Mukherjee, H.L. Wei, A. De, and T. DebRoy. Heat and fluid flow in additive manufacturing—part i: Modeling of powder bed fusion. *Computational Materials Science*, 150:304–313, 2018.
- [148] Habimana Jean Willy, Xinwei Li, Zhe Chen, Tun Seng Heng, Shuai Chang, Chun Yee Aaron Ong, Chaojiang Li, and Jun Ding. Model of laser energy absorption adjusted to optical measurements with effective use in finite element simulation of selective laser melting. *Materials & Design*, 157:24–34, 2018.
- [149] Qiang Chen, Gildas Guillemot, Charles-André Gandin, and Michel Bellet. Numerical modelling of the impact of energy distribution and marangoni surface tension on track shape in selective laser melting of ceramic material. *Additive Manufacturing*, 21:713–723, 2018.
- [150] Chien-Chou Tseng and Cheng-Jui Li. Numerical investigation of interfacial dynamics for the melt pool of ti-6al-4v powders under a selective laser. *International Journal of Heat and Mass Transfer*, 134:906–919, 2019.
- [151] Saad A. Khairallah, Andrew T. Anderson, Alexander Rubenchik, and Wayne E. King. Laser powder-bed fusion additive manufacturing: Physics of complex melt flow and formation mechanisms of pores, spatter, and denudation zones. *Acta Materialia*, 108:36–45, 2016.
- [152] Zekun Wang, Wentao Yan, Wing Liu, and Moubin Liu. Powder-scale multi-physics modeling of multi-layer multi-track selective laser melting with sharp interface capturing method. *Computational Mechanics*, 63:649–661, 04 2019.
- [153] Hui Chen, Qingsong Wei, Yingjie Zhang, Fan Chen, Yusheng Shi, and Wentao Yan. Powder-spreading mechanisms in powder-bed-based

- additive manufacturing: Experiments and computational modeling. *Acta Materialia*, 179:158–171, 2019.
- [154] Sofiane Benyahia, Madhava Syamlal, and Thomas O'Brien. Extension of hill-koch-ladd drag correlation over all ranges of reynolds number and solids volume fraction. *Powder Technology*, 162:166–174, 03 2006.
- [155] Alberto Di Renzo and Francesco Paolo Di Maio. Comparison of contact-force models for the simulation of collisions in dem-based granular flow codes. *Chemical Engineering Science*, 59(3):525–541, 2004.
- [156] A.B. Stevens and C.M. Hrenya. Comparison of soft-sphere models to measurements of collision properties during normal impacts. *Powder Technology*, 154(2):99–109, 2005.
- [157] Binqi Liu, Gang Fang, Liping Lei, and Wei Liu. A new ray tracing heat source model for mesoscale cfd simulation of selective laser melting (slm). *Applied Mathematical Modelling*, 79:506–520, 2020.
- [158] Carolin Körner, Andreas Bauereiß, and Elham Attar. Fundamental consolidation mechanisms during selective beam melting of powders. *Modelling and Simulation in Materials Science and Engineering*, 21(8):085011, 2013.
- [159] M.A. Russell, A. Souto-Iglesias, and T.I. Zohdi. Numerical simulation of laser fusion additive manufacturing processes using the sph method. *Computer Methods in Applied Mechanics and Engineering*, 341:163–187, 2018.
- [160] Saad A. Khairallah and Andy Anderson. Mesoscopic simulation model of selective laser melting of stainless steel powder. *Journal of Materials Processing Technology*, 214(11):2627–2636, 2014.
- [161] Richard Andreotta, Leila Ladani, and William Brindley. Finite element simulation of laser additive melting and solidification of inconel 718 with experimentally tested thermal properties. *Finite Elements in Analysis and Design*, 135:36–43, 2017.
- [162] M. Trautmann, M. Hertel, and U. Füssel. Numerical simulation of tig weld pool dynamics using smoothed particle hydrodynamics. *International Journal of Heat and Mass Transfer*, 115:842–853, 2017.
- [163] Jürgen Weirather, Vladyslav Rozov, M. Wille, Paul Schuler, Christian Seidel, Nikolaus A. Adams, and Michael F. Zaeh. A smoothed particle hydrodynamics model for laser beam melting of ni-based alloy 718. *Comput. Math. Appl.*, 78:2377–2394, 2019.
- [164] Yunji Qiu, Xiaofeng Niu, Tingting Song, Mengqing Shen, Wenqi Li, and Wenliang Xu. Three-dimensional numerical simulation of selective laser melting process based on sph method. *Journal of Manufacturing Processes*, 71:224–236, 2021.
- [165] Christoph Meier, Sebastian L. Fuchs, A. John Hart, and Wolfgang A. Wall. A novel smoothed particle hydrodynamics formulation for thermo-capillary phase change problems with focus on metal additive manufacturing melt pool modeling. *Computer Methods in Applied Mechanics and Engineering*, 381:113812, 2021.
- [166] Mohamadreza Afrasiabi, Christof Lüthi, Markus Bambach, and Konrad Wegener. Multi-resolution sph simulation of a laser powder bed fusion additive manufacturing process. *Applied Sciences*, 11(7):2962, Mar 2021.
- [167] Chang Park and T. Zohdi. Numerical modeling of thermo-mechanically induced stress in substrates for droplet based additive manufacturing processes. *Journal of Manufacturing Science and Engineering*, 141:1, 03 2019.
- [168] Jan-Philipp Fürstenau, Henning Wessels, Christian Weißenfels, and Peter Wriggers. Generating virtual process maps of slm using powder scale sph simulations. *Computational Particle Mechanics*, 7, 10 2019.
- [169] C.W Hirt and B.D Nichols. Volume of fluid (vof) method for the dynamics of free boundaries. *Journal of Computational Physics*, 39(1):201–225, 1981.
- [170] Wentao Yan, Wenjun Ge, Ya Qian, Stephen Lin, Bin Zhou, Wing Kam Liu, Feng Lin, and Gregory J. Wagner. Multi-physics modeling of single/multiple-track defect mechanisms in electron beam selective melting. *Acta Materialia*, 134:324–333, 2017.
- [171] David Adalsteinsson and James A. Sethian. A fast level set method for propagating interfaces. *Journal of Computational Physics*, 118:269–277, 1995.
- [172] Huan Qi, Jyotirmoy Mazumder, and Hyungson Ki. Numerical simulation of heat transfer and fluid flow in coaxial laser cladding process for direct metal deposition. *Journal of Applied Physics*, 100(2):024903, 2006.
- [173] Hyungson Ki, Jyoti Mazumder, and Pravansu S Mohanty. Modeling of laser keyhole welding: Part i. mathematical modeling, numerical methodology, role of recoil pressure, multiple reflections, and free surface evolution. *Metallurgical and materials transactions A*, 33(6):1817–1830, 2002.
- [174] Zhaoyang Liu and Huan Qi. Numerical simulation of transport phenomena for a double-layer laser powder deposition of single-crystal superalloy. *Metallurgical and Materials Transactions A*, 45(4):1903–1915, 2014.
- [175] J.U Brackbill, D.B Kothe, and C Zemach. A continuum method for modeling surface tension. *Journal of Computational Physics*, 100(2):335–354, 1992.
- [176] Zhengtao Gan, Gang Yu, Xiuli He, and Shaoxia Li. Surface-active element transport and its effect on liquid metal flow in laser-assisted additive manufacturing. *International Communications in Heat and Mass Transfer*, 86:206–214, 2017.
- [177] Alexis Queva, Gildas Guillemot, Clara Moriconi, Charlotte Metton, and Michel Bellet. Numerical study of the impact of vaporisation on melt pool dynamics in laser powder bed fusion - application to in718 and ti-6al-4v, additive manufacturing 35 (2020) 101249. *Additive Manufacturing*, page 101249, 05 2020.
- [178] J. Tan, Chao Tang, and C. Wong. A computational study on porosity evolution in parts produced by selective laser melting. *Metallurgical and Materials Transactions A*, 49, 06 2018.
- [179] Liu Cao. Numerical simulation of the impact of laying powder on selective laser melting single-pass formation. *International Journal of Heat and Mass Transfer*, 141:1036–1048, 10 2019.
- [180] K.Q. Le, C. Tang, and C.H. Wong. On the study of keyhole-mode melting in selective laser melting process. *International Journal of Thermal Sciences*, 145:105992, 2019.
- [181] Chunlei Qiu, Chinnapat Panwisawas, Mark Ward, Hector C. Basoalto, Jeffery W. Brooks, and Moataz M. Attallah. On the role of melt flow into the surface structure and porosity development during selective laser melting. *Acta Materialia*, 96:72–79, 2015.
- [182] Mohamad Bayat, Venkata Nadimpalli, David Pedersen, and J.H. Hattel. A fundamental investigation of thermo-capillarity in laser powder bed fusion of metals and alloys. *International Journal of Heat and Mass Transfer*, 166:120766, 02 2021.
- [183] Mohamad Bayat, Sankhya Mohanty, and Jesper Henri Hattel. Multiphysics modelling of lack-of-fusion voids formation and evolution in in718 made by multi-track/multi-layer l-pbf. *International Journal of Heat and Mass Transfer*, 139:95–114, 2019.
- [184] Y.S. Lee and W. Zhang. Modeling of heat transfer, fluid flow and solidification microstructure of nickel-base superalloy fabricated by laser

- powder bed fusion. *Additive Manufacturing*, 12:178–188, 2016. Special Issue on Modeling & Simulation for Additive Manufacturing.
- [185] Yu-Che Wu, Cheng-Hung San, Chih-Hsiang Chang, Huey-Jiuan Lin, Raed Marwan, Shuhei Baba, and Weng-Sing Hwang. Numerical modeling of melt-pool behavior in selective laser melting with random powder distribution and experimental validation. *Journal of Materials Processing Technology*, 254:72–78, 2018.
- [186] Mustafa Megahed, Hans-Wilfried Mindt, Narcisse N'Dri, Hongzhi Duan, and Olivier Desmaison. Metal additive-manufacturing process and residual stress modeling. *Integrating Materials and Manufacturing Innovation*, 5(1):61–93, 2016.
- [187] H. Mindt, Mustafa Megahed, Nicholas Lavery, Marc Holmes, and S.G.R. Brown. Powder bed layer characteristics: The overseen first-order process input. *Metallurgical and Materials Transactions A*, 47, 04 2016.
- [188] H.-W Mindt, Olivier Desmaison, Mustafa Megahed, Alonso Peralta, and J. Neumann. Modeling of powder bed manufacturing defects. *Journal of Materials Engineering and Performance*, 27, 09 2017.
- [189] Jonas Zielinski, Hans-Wilfried Mindt, Jan DÜchting, Johannes Henrich Schleifenbaum, and Mustafa Megahed. Numerical and experimental study of ti6al4v components manufactured using powder bed fusion additive manufacturing. *JOM*, 69(12):2711–2718, 2017.
- [190] A. Pinkerton. An analytical model of beam attenuation and powder heating during coaxial laser direct metal deposition. *Journal of Physics D*, 40:7323–7334, 2007.
- [191] Zhichao Liu, Hong-Chao Zhang, Shitong Peng, Hoyeol Kim, Dongping Du, and Weilong Cong. Analytical modeling and experimental validation of powder stream distribution during direct energy deposition. *Additive Manufacturing*, 30:100848, 2019.
- [192] L. Han, K. Phatak, and Frank Liou. Modeling of laser cladding with powder injection. *Metallurgical and Materials Transactions B*, 35:1139–1150, 01 2004.
- [193] Adrien Mouchard, Michael Pomeroy, Jeremy Robinson, Bryan McAuliffe, Simon Donovan, and David Tanner. An analytical method for powder flow characterisation in direct energy deposition. *Additive Manufacturing*, 42:101991, 2021.
- [194] A J Pinkerton and L Li. Rapid prototyping using direct laser deposition—the effect of powder atomization type and flowrate. *Proceedings of the Institution of Mechanical Engineers, Part B: Journal of Engineering Manufacture*, 217(6):741–752, 2003.
- [195] Wu Jiazhu, Tongwei Liu, Huanyu Chen, Fazhi Li, Haiying Wei, and Yi Zhang. Simulation of laser attenuation and heat transport during direct metal deposition considering beam profile. *Journal of Materials Processing Technology*, 270:92–105, 2019.
- [196] Jehnming Lin. Temperature analysis of the powder streams in coaxial laser cladding. *Optics & Laser Technology*, 31(8):565–570, 1999.
- [197] Wim Devesse, Dieter De Baere, and Patrick Guillaume. Modeling of laser beam and powder flow interaction in laser cladding using ray-tracing. *Journal of Laser Applications*, 27(S2):S29208, 2015.
- [198] S.Y. Wen, Y.C. Shin, J.Y. Murthy, and P.E. Sojka. Modeling of coaxial powder flow for the laser direct deposition process. *International Journal of Heat and Mass Transfer*, 52(25):5867–5877, 2009.
- [199] Christopher Katinas, Weixiao Shang, Yung C. Shin, and Jun Chen. Modeling Particle Spray and Capture Efficiency for Direct Laser Deposition Using a Four Nozzle Powder Injection System. *Journal of Manufacturing Science and Engineering*, 140(4), 02 2018. 041014.
- [200] Xiaoyi Guan and Yaoyao Fiona Zhao. Numerical modeling of coaxial powder stream in laser-powder-based directed energy deposition process. *Additive Manufacturing*, 34:101226, 2020.
- [201] O. O. Diniz Neto and R. Vilar. Physical–computational model to describe the interaction between a laser beam and a powder jet in laser surface processing. *Journal of Laser Applications*, 14(1):46–51, 2002.
- [202] Yan-Lu Huang, Jian Liu, Nai-Heng Ma, and Jian-Guo Li. Three-dimensional analytical model on laser-powder interaction during laser cladding. *Journal of Laser Applications*, 18(1):42–46, 2006.
- [203] Jichang Liu, Lijun Li, Yuanzhong Zhang, and Xiaozhu Xie. Attenuation of laser power of a focused gaussian beam during interaction between a laser and powder in coaxial laser cladding. *Journal of Physics D: Applied Physics*, 38:1546, 05 2005.
- [204] Marco Picasso, C. Marsden, J. Wagniere, A. Frenk, and M. Rappaz. A simple but realistic model for laser cladding. *Metallurgical and Materials Transactions B*, 25:281–291, 04 1994.
- [205] Wim Devesse, Dieter De Baere, and Patrick Guillaume. Modeling of laser beam and powder flow interaction in laser cladding using ray-tracing. *Journal of Laser Applications*, 27(S2):S29208, 2015.
- [206] W.-B Li, Hans Engström, John Powell, Z. Tan, and C. Magnusson. Redistribution of the beam power in laser cladding by powder injection. *Lasers in Engineering*, 5:175–183, 01 1996.
- [207] Mazher Mohammed. A review of laser engineered net shaping (lens) build and process parameters of metallic parts. *Rapid Prototyping Journal*, 26, 03 2020.
- [208] Junhua Wang, Zhen Zhang, Fuzhu Han, Shu-fan Chen, and Weisheng Ying. Modeling of laser power attenuation by powder particles for laser solid forming. *Procedia CIRP*, 95:42–47, 01 2020.
- [209] Christopher Katinas, Tyler Throop, Yung Shin, and Alex Frank. Laser cladding of stellite-6 with a coaxial nozzle via modeling and systematic experimental investigations. *The International Journal of Advanced Manufacturing Technology*, 113:1–17, 03 2021.
- [210] Jian Zhang, Lin Yang, Zhuoyuan Li, Qingmao Zhang, Manjiang Yu, Chaolong Fang, and Haibing Xiao. Transport phenomenon, flow field, and deposition forming of metal powder in the laser direct deposition with designed nozzle. *The International Journal of Advanced Manufacturing Technology*, 114, 05 2021.
- [211] David Svetlizky, Mitun Das, Baolong Zheng, Alexandra Vyatskikh, Susmita Bose, Amit Bandyopadhyay, Julie Schoenung, Enrique Lavernia, and Noam Eliaz. Directed energy deposition (ded) additive manufacturing: Physical characteristics, defects, challenges and applications. *Materials Today*, 06 2021.
- [212] A. Frenk, Mehrdad Vandyoussefi, J. Wagnière, W. Kurz, and Amedee Zryd. Analysis of the laser-cladding process for stellite on steel. *Metallurgical and Materials Transactions B*, 28:501–508, 06 1997.
- [213] Zhaoyang Liu, Liang Jiang, Zi Wang, and L. Song. Mathematical modeling of transport phenomena in multi-track and multi-layer laser powder deposition of single-crystal superalloy. *Metallurgical and Materials Transactions A*, 49:6533–6543, 2018.
- [214] Tsan-Hsing Shih, William W. Liou, Aamir Shabbir, Zhigang Yang, and Jiang Zhu. A new  $k - \epsilon$  eddy viscosity model for high reynolds number turbulent flows. *Computers & Fluids*, 24(3):227–238, 1995.
- [215] F. R. Menter. Two-equation eddy-viscosity turbulence models for engineering applications. *AIAA Journal*, 32(8):1598–1605, 1994.
- [216] A. Haider and O. Levenspiel. Drag coefficient and terminal velocity of spherical and nonspherical particles. *Powder Technology*, 58(1):63–70,

- 1989.
- [217] Long He, Danesh K. Tafti, and Krishnamurthy Nagendra. Evaluation of drag correlations using particle resolved simulations of spheres and ellipsoids in assembly. *Powder Technology*, 313:332–343, 2017.
  - [218] Simon Morville, Muriel Carin, Patrice Peyre, Myriam Gharbi, Denis Carron, Philippe Le Masson, and Rémy Fabbro. 2d longitudinal modeling of heat transfer and fluid flow during multilayered direct laser metal deposition process. *Journal of Laser Applications*, 24(3):032008, 2012.
  - [219] Wei Ya, B. Pathiraj, and Shaojie Liu. 2d modelling of clad geometry and resulting thermal cycles during laser cladding. *Journal of Materials Processing Technology*, 230:217–232, 2016.
  - [220] Godfrey C. Onwubolu, J.Paulo Davim, Carlos Oliveira, and A. Cardoso. Prediction of clad angle in laser cladding by powder using response surface methodology and scatter search. *Optics & Laser Technology*, 39(6):1130–1134, 2007.
  - [221] Ondřej Nenadl, Václav Ocelík, Armin Palavra, and Jeff Th.M. De Hosson. The prediction of coating geometry from main processing parameters in laser cladding. *Physics Procedia*, 56:220–227, 2014. 8th International Conference on Laser Assisted Net Shape Engineering LANE 2014.
  - [222] HL Wei, FQ Liu, WH Liao, and TT Liu. Prediction of spatiotemporal variations of deposit profiles and inter-track voids during laser directed energy deposition. *Additive Manufacturing*, 34:101219, 2020.
  - [223] Simeng Li, Hui Xiao, Keyang Liu, Wenjia Xiao, Yanqin Li, Xu Han, Jyoti Mazumder, and Lijun Song. Melt-pool motion, temperature variation and dendritic morphology of inconel 718 during pulsed- and continuous-wave laser additive manufacturing: A comparative study. *Materials & Design*, 119:351–360, 2017.
  - [224] W. Zhang, Cheolhee Kim, and Tarasankar Debroy. Heat and fluid flow in complex joints during gas metal arc welding—part i: Numerical model of fillet welding. *Journal of Applied Physics*, 95:5210–5219, 05 2004.
  - [225] V. Manvatkar, A. De, and T. DebRoy. Heat transfer and material flow during laser assisted multi-layer additive manufacturing. *Journal of Applied Physics*, 116(12), 9 2014.
  - [226] Mohamad Bayat, Venkata K. Nadimpalli, Francesco G. Biondani, Sina Jafarzadeh, Jesper Thorborg, Niels S. Tiedje, Giuliano Bissacco, David B. Pedersen, and Jesper H. Hattel. On the role of the powder stream on the heat and fluid flow conditions during directed energy deposition of maraging steel—multiphysics modeling and experimental validation. *Additive Manufacturing*, 43:102021, 2021.
  - [227] Stephen Lin, Zhengtao Gan, Jinhui Yan, and Gregory J. Wagner. A conservative level set method on unstructured meshes for modeling multiphase thermo-fluid flow in additive manufacturing processes. *Computer Methods in Applied Mechanics and Engineering*, 372:113348, 2020.
  - [228] C. Wang, X.P. Tan, S.B. Tor, and C.S. Lim. Machine learning in additive manufacturing: State-of-the-art and perspectives. *Additive Manufacturing*, 36:101538, 2020.
  - [229] *A Review of Machine Learning Applications in Additive Manufacturing*, volume Volume 1: 39th Computers and Information in Engineering Conference of *International Design Engineering Technical Conferences and Computers and Information in Engineering Conference*, 08 2019. V001T02A040.